First global assessment of the Eddy-Diffusivity Mass-Flux (EDMF) parameterization for oceanic convection in NEMO: implications for global temperature and surface heat fluxes

Violaine Piton[1], Hervé Giordani[2], Romain Bourdallé-Badie[1], Charles Pelletier[3]

[1]Mercator Ocean International, Toulouse, France
[2]CNRM/CNRS, UMR-3589, Météo-France, Toulouse, France
[3]European Centre for Medium-Range Weather Forecasts, Bonn, Germany

Correspondence to: Violaine Piton (vpiton@mercator-ocean.fr)

Abstract. The Eddy-Diffusivity Mass-Flux (EDMF) parameterization provides a unified framework to represent both local (diffusive) and non-local (convective) vertical mixing in the ocean. While EDMF has been evaluated in idealized and regional configurations, its performance in global ocean models has not yet been assessed. We present the first global-scale evaluation of the EDMF scheme implemented in NEMO and compare it with the widely used Enhanced Vertical Diffusion (EVD) and Mixed Layer Penetration (MLP) parameterizations. Three global 1/4° simulations for 1999–2020 are analyzed, focusing on convective regimes, upper-ocean temperature and mixed-layer depth.

EDMF successfully reproduces both shallow diurnal convection in the tropics and deep wintertime convection in subpolar regions, with modelled plume timing, penetration depth and vertical velocities consistent with available observations. In the tropics, EDMF captures the observed penetrative cooling and depth variability of nocturnal cold plumes, in contrast to the instantaneous adjustment produced by EVD. In deep-convection regions such as the Labrador Sea, EDMF simulates realistic interannual variability in convective depth and intensity.

The improved representation of convective regimes leads to a ~30% reduction in global upper-ocean (0-700m) temperature biases in EDMF compared to EVD-based simulations. Changes in latent heat loss, driven by SST differences, dominate the associated changes in net surface heat flux between EDMF and EVD simulations, corresponding to ~6.5% of the global average net climatological surface heat balance.

These findings demonstrate that EDMF provides a more physically consistent representation of oceanic convection and offers an alternative to traditional and empirical EVD- and MLP- based approaches.

1 Introduction

By communicating heat, mass and momentum between the atmosphere and ocean interior, the ocean boundary layer (OBL) plays a central role in the evolution of the global ocean heat budget, water-mass formation and air-sea carbon exchange. Vertical mixing within the OBL is typically categorized into two regimes: (i) diffusive mixing, driven by small-scale eddies that transports properties down their local mean gradient, and (ii) non-diffusive mixing, associated with organized large-scale eddies such as convective plumes, which can induce counter-gradient and non-local transport.

Convective plumes are often triggered by surface water cooling or salinification which generate hydrostatic instabilities (e.g. increase in surface water density), resulting in downward motion of buoyant plumes. Depending on factors such as the strength of the buoyancy forcing and the ocean stratification, these convective plumes may remain confined to the mixed layer or penetrate to abyssal depths. The forcing also determines the timescale of convective events, which can range from diurnal to seasonal or even interannual (Marshall & Schott, 1999; Morales Maqueda et al. 2004; Vreugdhenil and Gayen, 2021).

In tropical and subtropical regions, daytime solar heating generates a warm, stably stratified surface layer in the upper few meters. At night, surface cooling, often coupled with wind forcing, destabilizes the upper ocean and initiates convective overturning that erodes the diurnal warm layer (Woolnough et al., 2007; Bellenger & Duvel, 2009; Moum et al., 2023). These nocturnal convective plumes are typically shallow, extending only a few tens of meters, with deepest penetrations near the equator (Masich et al., 2021; Moum et al., 2023; Wenegrat & McPhaden, 2015).

At higher latitudes, intense surface heat loss during winter drives deep convection events that can reach depths of several hundred to thousand meters. Recurrent wintertime deep convection sites have been identified in the Greenland, Labrador, and Irminger Seas (Våge et al., 2009; Frajka-Williams et al., 2014; Piron et al., 2017), as well as in the Weddell Sea (Gordon et al., 1978) and the Mediterranean Sea (Schott et al., 1996; Houpert et al., 2015).

By generating large-scale non-diffusive mixing, these two distinct convective regimes (shallow diurnal and deep seasonal) significantly deepen and sustain the upper-ocean mixed layer (Vreugdhenil and Gayen. 2021). Accurately representing convection occurring in the OBL in general circulation models (GCMs) is therefore essential for reliable representation of the mixed layer depth (MLD), and consequent implications on heat storage and global water-mass transport (Fox-Kemper et al. 2019).

For an accurate representation of the total turbulent fluxes within the OBL, both contributions of the diffusive and non-diffusive mixing must be represented. However, the small horizontal scales of the diffusive (O(~1-10)m) and non-diffusive (O(~10-1000)m) turbulent mixing can not be explicitly resolved in ocean GCMs, as these processes occur at subgrid scales and act primarly in the vertical direction and therefore must be parameterized.

The traditional way to parameterize the turbulent diffusive mixing in GCMs is through the Eddy-Diffusivity (ED) based on a K-gradient approach (Gaspar et al., 1990). This latter estimates the vertical turbulent flux of a field ψ as $\overline{w'\psi'} = -K_z \frac{\partial \psi}{\partial z}$, where K_z ($m^2\ s^{-1}$) is the ED coefficient. Though successfully representing the

OBL diffusing mixing, the ED method by itself fails at representing the mixing induced by large eddies because the parcels move regardless of the local gradient.

In order to include the non-diffusive mixing that propagates counter-gradient of the stratification, several modifications were introduced into ED formulations. As for example, Large et al. (1994) added the effect of non-diffusive convective mixing to the local K-theory through a non-local term (KPP). An exhaustive and descriptive inventory is provided by Garanaik et al. (2024), though none of these schemes explicitly represent the convective mixing. This is also the case for the Enhanced Vertical Diffusion (EVD) parameterization traditionally used in the NEMO ocean model. This approach mimics convective mixing by artificially enhancing vertical diffusivity by assigning large K_z values wherever static instability is detected in the density profile, thereby representing convection as very strong local turbulent vertical diffusion (Madec et al., 2019).

To address this shortcoming, the Eddy-Diffusivity and Mass-Flux (EDMF) parameterization has been more recently introduced in NEMO (Giordani et al., 2020). EDMF unifies a local downgradient diffusive component (ED) with an explicit nonlocal mass-flux (MF) component that represents the vertical advective transport associated with convective plumes.

As such, EDMF has attracted increasing attention as a promising alternative for representing oceanic convection in coarse-resolution models. The EDMF parameterization within NEMO has already been tested and validated in 1-D scenarios within the Gulf of Lions (Mediterranean Sea) and at the PAPA station (northern Pacific Ocean) (Giordani et al., 2020), and in 3-D regional scenarios in the Maud Rise region (off the north coasts of Antarctica) (Gülk et al., 2024). Similar mixing schemes using the MF concept have been used and validated in single column test cases (Garanaik et al. 2024, Perrot et al. 2024, Perrot and Lemarié 2025), or implemented in the code Oceananigans (Ramadhan et al. 2020). To the authors' knowledge, the EDMF parameterization has never been tested in a global ocean model configuration before.

Under the framework of the NEMO Consortium, which ensures the sustainable development of the NEMO platform to support oceanographic research, forecasting, and climate studies, this paper has four main objectives:

- To evaluate the EDMF parameterization in a global NEMO simulation at ¼° resolution, by assessing key variables such as temperature, salinity, ocean transport, and mixed layer depth (MLD);
- To compare the performance of the EDMF scheme against the widely-used EVD parameterization in representing these quantities;
- To assess the ability of the EDMF scheme to represent both shallow diurnal and deep seasonal convective regimes;
- To quantify the contribution of convection to the global net surface fluxes.

2 Methods

2.1 Model and simulations performed: shared features

We analyze the outputs of three NEMO standalone simulations which differ one from another only by their respective choice of vertical diffusive and/or convection parameterizations. In this subsection, we describe the experimental design shared by all three experiments.

We use the ocean-sea ice coupled model of the Nucleus for European Modelling of the Ocean (NEMO) version 4.2 (Madec et al., 2022), coupled with the Sea Ice modelling Integrated Initiative (SI3, Vancoppenolle et al., 2023), with its default settings and 5 ice thickness categories. Simulations are performed on a 1/4° global tripolar grid with 75 vertical ocean z levels, whose thickness increases non-uniformly from 1 m at the surface to 10 m at 100 m depth, and up to 200 m near the bottom. Atmospheric forcing is provided by the ERA5 reanalysis at hourly frequency (Hersbach et al., 2020) via the XYZ bulk formula. The eddy-induced velocities parameterization of Gent and McWilliams (1990) is activated, enabling the representation of the full mesoscale turbulence associated with eddies in this "eddy-permitting" configuration. The penetration of solar radiation is prescribed following the algorithm of Morel et al. (1988). The monthly climatology field of surface chlorophyll of Sathyendranath et al. (2019) is prescribed.

All three simulations are conducted over the 1999-2020 period. The ocean and ice fields are initialized on October 1, 1999 using the state-of-the-art Global Reanalysis Ensemble Product (GREP) at 1/4° resolution (https://doi.org/10.48670/moi-00024) provided by the Copernicus Marine Service. Following a five-year spin-up period, the model outputs were analyzed over a 16-year period spanning 2005–2020 corresponding to the Argo program period.

2.2 Vertical mixing parameterization options

We now focus more specifically on the parametrization pertaining to vertical mixing. For representing vertical diffusive mixing, all three experiments employ a "1.5th-order" turbulent-kinetic-energy (TKE) closure scheme initially proposed by Blanke and Delecluse (1993). The eddy diffusivity K_z is then diagnosed from the TKE. In one of our simulations, the TKE scheme is complemented with the so-called "mixed-layer penetration" (MLP) scheme, increasing the upper ocean TKE to account for the effects of near-inertial oscillations and surface gravity wave breaking (Rodgers et al. 2014). The MLP scheme adds a TKE source term (in our case, 5% of the surface TKE), distributed vertically with an exponentially decreasing shape function from the surface down to depths ranging from 0.5m (at the Equator) down to 40m (at higher latitudes in both hemispheres). Introduced as an ad hoc, empirically-based parameterization, the MLP was implemented to deepen the mixed layer depth (MLD), which was commonly found to be too shallow in the Southern Ocean during summer under windy conditions (Rodger et al., 2014). This scheme is active by default in NEMO4.2, as it has been shown to improve the realism of MLD in the Southern Ocean, Arctic region and open-water areas (Calvert and Siddorn, 2013; Rodgers et al., 2014; Heuzé et al., 2015; Storkey et al., 2018; Allende et al., 2024).

NEMO's current default option for representing convective vertical mixing is the "enhanced vertical diffusivity" (EVD) parametrization (Madec et al., 2019). When the stratification between two vertically adjacent cells is unstable (i.e., when the density increases with depth), the EVD scheme overrides the TKE scheme by setting the

eddy diffusivity to a large constant value (up to $K_z = 10^2\ m^2 s^{-1}$), very effectively mixing both cells. Under stable stratification, the EVD parametrization leaves K_z unchanged and is thus inactive. In essence, the EVD represents nonlocal vertical mixing via a fundamentally local mechanism (diffusion, i.e., $K_z \partial_z T$), albeit employing diffusivities large enough to mimic nonlocal effects. The EVD scheme is used in two of our three experiments.

As an alternative to the EVD parameterization, NEMO4.2 now also allows the use of the mass-flux parameterization to represent the convective vertical mixing with bespoke numerics (see Giordani et al., 2020). Inspired by atmospheric convective parameterizations (Siebesma et al., 2007), it explicitly represents convective plumes nested within their surrounding environment and is by construction nonlocal. The mass-flux parametrization aims solely at representing convective mixing and is typically combined with the aforementioned TKE closure, accounting for diffusive mixing. The combination of both parametrizations is hereinafter referred to as Eddy-Diffusivity Mass-Flux (EDMF) parametrization. One of our experiments uses a version of the EDMF parametrization which, compared to Giordani et al. (2020), was revisited for the global ocean. EDMF parameterization is designed to respond to density instabilities regardless of their origin, including, for example, those induced by surface cooling or salinification, Ekman boundary fluxes, or coastal downwelling.

The main characteristics of the Mass-Flux (MF) component of EDMF scheme (Giordani et al., 2020) are briefly recalled here. Note that the present EDMF formulation is applied for all convective regimes, without using regime-specific parameterizations or coefficients. The surface buoyancy flux is used to derive the fractional convective area of the plume, from which the plume is initiated. The plume velocity (w_p) is computed by integrating the equation:

$$\left(\frac{1}{2}+\alpha\right)\frac{\partial w_p^2}{\partial z} = a_1 F_b - \alpha g \frac{\rho_p}{p_h} w_p^2 \qquad (1)$$

using the gravitational acceleration g, the plume buoyancy acceleration F_b, the surface-referenced potential density of the plume ρ_p, the hydrostatic pressure p_h and the coefficients a_1 and α. The value $a_1 = 1$ was diagnosed from Large Eddy Simulations in the atmosphere (Siebesma et al., 2003) and $\alpha = 0.2$ produced the best results in the EDMF 1-D test cases. The coefficient $\alpha g \frac{\rho_p}{p_h}$ represents the resistance term associated with the non-hydrostatic pressure perturbation applied to downward parcels. In our configuration, we use $\alpha = 1$ to prevent any damping of this resistance term.

The computation of the plume convective area a_p is determined as:

$$\frac{1}{a_p}\frac{\partial a_p}{\partial z} = -\mathcal{L} + \epsilon_{a_p} - \delta_{a_p} \quad \text{with} \quad \mathcal{L} = \frac{1}{w_p}\frac{\partial w_p}{\partial z}, \qquad (2)$$

These quantities correspond to vertical decay scale, as described in Giordiani et al. (2020). The shape of the vertical velocity in the convective area is such that it increases in the upper part ($\mathcal{L} > 0$) and decreases in the deeper part ($\mathcal{L} < 0$) of the plume.

In Eq. 2, the entrainment (ϵ_{a_p}) and detrainment (δ_{a_p}) rates between the plume and the environment are expressed as:

$$\epsilon_{a_p} = \beta_1 \, \mathrm{Max}(0, \mathcal{L})$$
$$\delta_{a_p} = -\beta_2 \, \mathrm{Min}(0, \mathcal{L}) \tag{3}$$

with the coefficients $\beta_1 = \beta_2 = 0.9$ (Rio et al. 2010, Giordani et al. 2020).

On the other hand, the plumes properties (ψ_p) which include the potential temperature (T_p) and the salinity (S_p) are determined as:

$$\frac{\partial \psi_p}{\partial z} = -\epsilon_\psi (\psi_p - \psi), \tag{4}$$

with the lateral entrainment rate ϵ_ψ between the plume and the environment computed as:

$$\epsilon_\psi = \left| \frac{1}{w_p} \frac{\partial w_p}{\partial z} \right| + \epsilon_g. \tag{5}$$

For consistency with ϵ_{a_p} and δ_{a_p}, we introduce a coefficient β in the computation of ϵ_ψ so that:

$$\epsilon_\psi = \beta \, \mathrm{Max}(0, \mathcal{L}) + \epsilon_g, \tag{6}$$

with $\beta = \beta_1 = \beta_2 = 0.9$, and the background entrainment rate ϵ_g equal to 0.001 (Giordani et al. 2020, Gülk et al. 2024).

Lastly, the initialization of T_p at the surface was originally coded to be equal to the surface temperature of the environment (T) at the same time step. In this study, to allow convection triggering with $T_p < T$, we modified the initialization so that the surface T_p is now set equal to surface T at the following half time step. This temperature increment is an estimate of the temperature difference between the convective plumes and their surrounding environment in the model grid-mesh. NEMO uses a leapfrog time-stepping scheme. The surface flux is evaluated at the half time step, which allows it to be used at the temporal center of the model time step.

As mentioned above, the vertical mixing parameterization choice distinguishes our three experiments one from another, for which Table 1 provides an overview. In our study, TKE+EVD can be considered as a "minimal" control experiment; TKE+MLP+EVD as a control experiment with settings that NEMO usually employ (including the ad-hoc MLP parametrization); EDMF is the new framework we are evaluating. The aim of the present study is to improve the representation of the vertical physics in the model, and ultimately, its ability to

reduce systematic biases. However, this capability only becomes apparent after an online re-calibration of the parameterizations (Hourdin et al., 2021, 2023).

Simulation	Diffusion	MLP?	Convection
TKE+EVD	TKE	No	EVD
TKE+MLP+EVD	TKE	Yes	EVD
EDMF	TKE	No	Mass-flux

Table 1: Summary of conducted experiments.

We compute the temperature trend from the divergence of the diffusive (∂zF_{diff}), convective (∂zF_{conv}) and total (∂zF_{tot}) vertical heat fluxes in EDMF simulation, as:

$$\partial_z F_{diff} = -\frac{\partial}{\partial z}\left(-K_z \frac{\partial T}{\partial z}\right)$$

$$\partial_z F_{conv} = -\frac{\partial}{\partial z}\left(\frac{\partial MF(T_p - T)}{\partial z}\right) \quad (7)$$

with the mass flux defined as $MF = a_p w_p$.

In the case of EDMF simulation: $\partial_z F_{tot} = \partial zF_{diff} + \partial_z F_{conv}$; whereas in the case of the EVD simulation: $\partial_z F_{tot} = \partial zF_{diff}$.

2.3 Observational dataset for simulations evaluation

The modeled sea surface temperature (SST) is compared to SST data from OSTIA (Operational Sea Surface Temperature and Sea Ice Analysis, SST_GLO_SST_L4_NRT_OBSERVATIONS_010_001, 2023; https://doi.org/10.48670/moi-00165), while the modeled vertical profiles of temperature are compared to in situ measurements from ARMOR and CORA-REP (INSITU_GLO_PHYBGCWAV_DISCRETE_MYNRT_013_030, 2024; https://doi.org/10.48670/moi-00036). From the hourly model outputs, the model equivalents of the observations are calculated using temporal and spatial interpolations. The bias and root mean square deviation (RMSD) are then calculated within 3° × 3° grid boxes to ensure statistical robustness by minimizing the risk of having too few in situ observations within smaller boxes.

Modeled monthly mixed-layer depth (MLD) climatologies are compared to the MLD climatology of de Boyer Montégut (2024), derived from temperature and salinity profiles collected between January 1970 and December 2021 from the Argo program, the NCEI-NOAA World Ocean Database and ice-tethered profilers. The MLD for each profile is computed using the threshold density criterion, following de Boyer Montégut et al. (2004), consistent with the MLD computation used in NEMO. This profile-based MLD has been recommended for the evaluation of global ocean models, as in OMIP (Tréguier et al. 2023). The observational climatology has a

spatial resolution of 1° × 1°, so the modeled MLD climatologies are resampled to this resolution for accurate comparison.

Modeled hourly near-surface temperatures are evaluated against in situ observations from the standard operational Tropical Atmosphere Ocean (TAO) surface mooring, maintained by the National Data Buoy Center (NDBC), located at 2°S, 140°W. The data were collected and made freely available by NOAA/NDBC. From February 2017 to June 2018, this mooring was additionally equipped with enhanced vertical resolution temperature sensors, providing measurements every 5 meters from the surface to 40 meters depth, and every 10 meters between 40 and 60 meters depth, at a 10-minute sampling interval. For comparison with model output, observational data were temporally averaged to a 1-hour frequency.

We compare the modeled Atlantic Meridional Overturning Circulation (AMOC) with the observed RAPID-MOCHA monitoring array at 26.5°N, which monitored the AMOC volume transport since April 2004 (https://rapid.ac.uk/data). The modeled AMOC computations are performed with the cdftools package (cdfmoc; https://meom-group.github.io/doc/CDFTOOLS/#PACKAGE-DESCRIPTION)

Seasonal modelled sea-ice concentration for the Arctic and Antarctic regions are compared to the GCOM-W1 product (Global AMSR Sea Ice Concentration, OSI SAF, 2017; https://dx.doi.org/10.15770/EUM_SAF_OSI_NRT_2023) derived from AMSR-2 satellite measurements and processed by the EUMETSAT OSISAF.

3 EDMF scheme evaluation

In this section, we first describe the spatio-temporal occurrences of the EDMF scheme and we detail the physical properties of the modeled convective plumes under different convective regimes. We then evaluate the performance of the simulation using the EDMF scheme in reproducing observed temperature patterns and MLD cycles, and we compare its accuracy to that of the simulations employing the EVD scheme (TKE+EVD and TKE+MLP+EVD simulations). Additional analysis of the EDMF performances in reproducing the Atlantic meridional overturning circulation *(*AMOC) is available in Text S1 and Fig. S8 of the SI.

3.1 EDMF scheme occurrence

We assess the occurrence of the MF component of the EDMF scheme by analyzing climatological (2005-2020) fields of daily plume vertical velocities (w_p) outputs from the EDMF simulation, as positive w_p indicate the presence of convective plumes.

This analysis shows that the MF component is active year-round in the tropical ocean (30°S–30°N), where it is confined to shallow depths (<100 m) (Fig. 1a–h). This convective activity is typical of the diurnal shallow convective regime that occurs in the tropics and subtropics at night due to the combination of wind and nighttime surface cooling (Shay and Gregg, 1986). During boreal winter, the MF component is activated in the northern hemisphere (Fig. 1e), whereas activation shifts to the southern hemisphere during austral winter (Fig.

1g), reflecting the seasonality of convective events. Deep convective activities (>500 m) are depicted in the northern Atlantic (Labrador and Irminger Seas) and southwestern Pacific near the Drake passage during boreal and austral winter, respectively (Fig. 1i–l). These regions are known as the few sites of the ocean where seasonal wintertime deep convection has been observed (Yashayaev and Loder, 2017; Behrens et al., 2016).

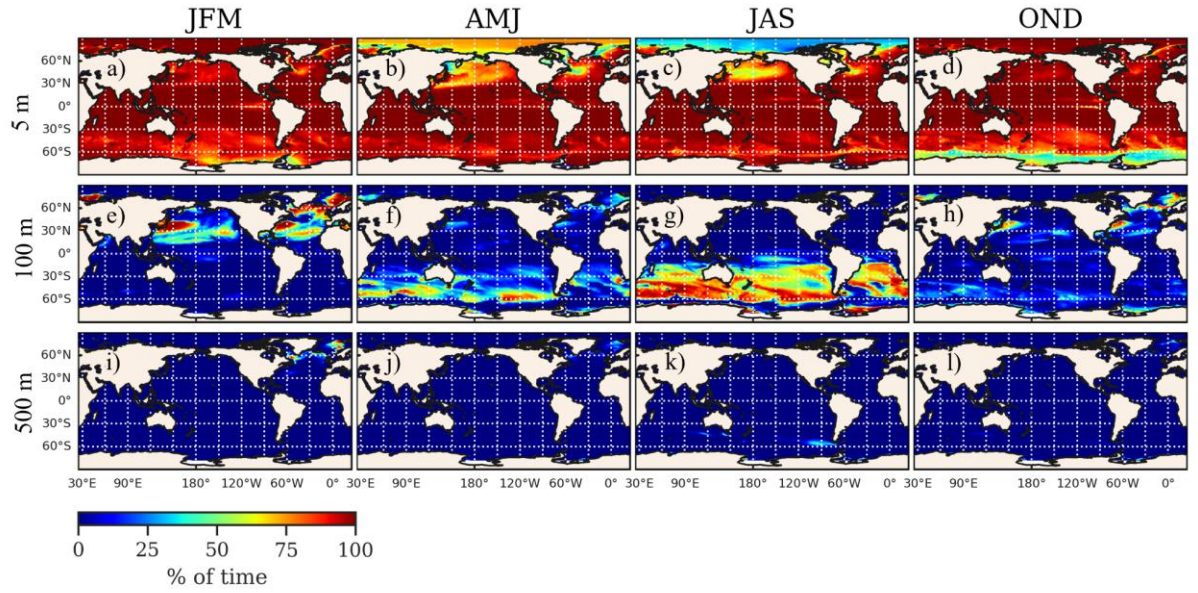


Figure 1: Seasonal activity of the MF component, as depicted as positive values of w_p averaged over the 2005-2020 period, at 5 (a-d), 100 (e-h) and 500 m depth (i-l) in terms of percentage (%) of time per month.

3.1.1 Deep-seasonal convection

Model outputs at 1-hour temporal resolution are analyzed at the mooring site (56.53°N, 52.65°W), located in the deep convective region of the Labrador Sea. Figure 2a presents the time series of surface net heat flux and vertical velocity of plumes (w_p) over four consecutive years (2011–2015). Each year, a gradual deepening and intensification of w_p is observed from late summer into autumn (August to November), associated with the seasonal transition from positive to negative surface heat flux. As winter progresses (December), the intensification of negative heat flux triggers the onset of deep convection (depths > 500 m), marked by a rapid increase in both depth and magnitude of w_p. The deep convection season typically stops in early spring (April), associated with the transition from negative to positive surface net heat flux.

However, substantial interannual variability in the intensity of the convection is observed (Fig. 2a). During the winter of 2012–13, the convective season was relatively short (late January to mid-March) and weak, with w_p reaching a maximum depth of ~900 m and peak values of ~5 cm s^{-1}. In contrast, the winter of 2014–15 was marked by an early onset of convection (beginning in December), which persisted through mid-April, reaching depths up to ~2000 m and w_p > 8 cm s^{-1}. Apart from major convective events, wintertime MLDs observed in the Labrador Sea typically range between 500 and 1500 m (Kieke and Yashayaev, 2015), consistent with the modelled maximum plume depths during the winters of 2011-12, 2012-13 and 2013-14 (Fig. 2a). The winter

2014-15 has been identified as a major deep convection event, occurring in both the Labrador and Irminger Seas (Piron et al. 2017), with depths comparable to those observed during 1993-1995 of ~2300 m (Kieke and Yashayaev, 2015). The modelled convective depths during winter 2014-15 are consistent with Argo-derived MLDs in the Labrador Sea, which ranged from 1000 to 1800 m during March-April 2015 (Piron et al. 2017). The modelled w_p also fall within the range of the few available observational estimates of w_p, such measurements remain scarce because of the difficulty to sample small oceanic vertical velocities. Using gliders deployed in the Labrador Sea during winter 2022, Clément et al. (2024) reported maximum w_p values of 4.6 cm s^{-1} and MLDs reaching 1000 m. These values indicate moderate convective conditions, consistent with the modelled values for the winter 2011-12 which presents moderate conditions compared to winters 2012-13 and 2014-15 (Fig. 2a).

Daily model outputs at the model grid cell containing the mooring site 56.53°N, 52.65°W are used to calculate the temperature trend from the divergence of the diffusive (∂zF_{diff}), convective (∂zF_{conv}) and total (∂zF_{tot}) vertical heat fluxes (Eq. 7; Fig. 2b). ∂zF_{diff} is nearly negligible over most of the water column, except for a weak signal close to the surface during the summers (Fig. 2b). Consequently, the vertical structure of ∂zF_{tot} is almost entirely determined by the convective contribution, ∂zF_{conv}. This illustrates that the deep response of the total vertical heat flux in the EDMF simulation is primarily associated with the mass-flux component rather than with diffusive mixing. Time series of ∂zF_{tot} and ∂zF_{diff} for the two EVD simulations are provided in Fig. S1, using the same location and time period, to compare the intensity and vertical extent of these fluxes under the same surface forcing.
Winter 2011/12 exhibits a deeper penetration of ∂zF_{tot} than in Fig. 2a, owing to the different spatial sampling used in the two panels. Fig. 2a uses hourly outputs at the mooring location, whereas Fig. 2b uses daily outputs at the model grid cell encompassing the mooring. Given the strong spatial variability of convection in the Labrador Sea, differences in the diagnosed penetration depth are therefore expected.

Hourly profiles of the modelled convective plumes characteristics for March 15, 2015, are shown in Fig. 2b-f. At the surface, negative heat fluxes trigger and maintain colder-than-environment plume temperatures ($T_p < T_{env}$, Fig. 2e) throughout, resulting in denser-than-environment plume waters ($\rho_p > \rho_{env}$, Fig. 2d). The plume convective areas (a_p), derived from surface buoyancy fluxes, are provided in Fig. 2c. As the plumes propagate downward and remain denser than their environment waters ($\rho_p > \rho_{env}$), they accelerate according to the work of the buoyancy force, reaching vertical velocities up to 8 cm s^{-1} while their a_p gradually shrink.
At the depth of neutral buoyancy—where plume and environment densities become equal ($\rho_p = \rho_{env}$), around ~1000 m—the plumes begin to decelerate, accompanied by an increase in a_p (their expansion). Below this level, as the plume waters become lighter than the environment waters ($\rho_p < \rho_{env}$), the plumes lose their gain buoyancy and eventually stops ($w_p = 0$) at depths of ~ 1700–2000 m.

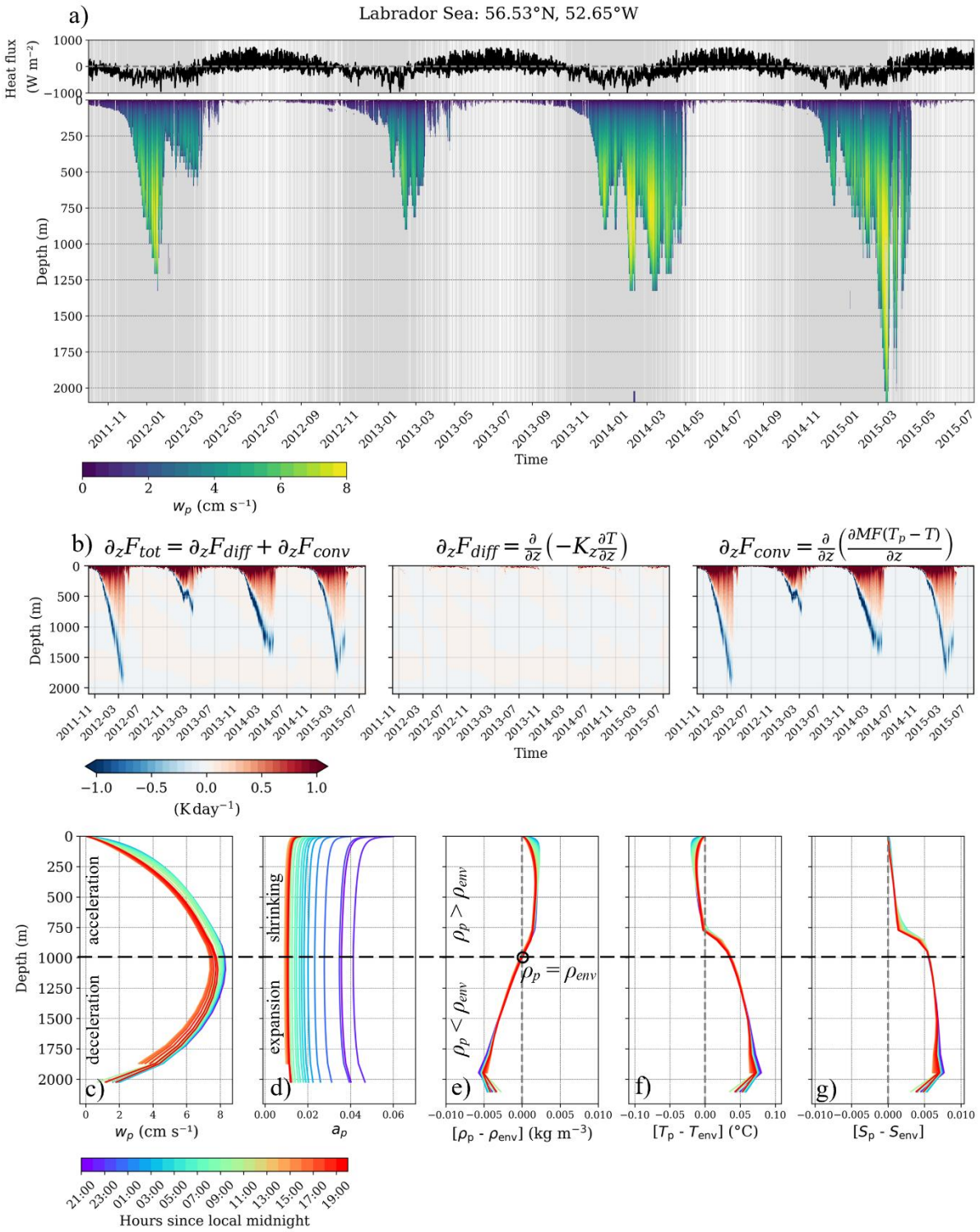


Figure 2: (a) Hourly time series of surface net heat flux (W m^{-2}) and plume w_p (cm s^{-1}) spanning October 2011 to July 2015 at mooring location 56.53°N, 52.65°W in the Labrador Sea. (b) Daily time series of temperature trend (K day^{-1}) from the divergence of the total ($\partial z F_{tot}$), diffusive ($\partial z F_{diff}$) and convective ($\partial z F_{conv}$) heat flux from EDMF simulation. Fluxes are computed at the model grid cell containing the mooring location and over the same time window as shown in (a). 24-hours profiles of (c) w_p, (d) a_p, (e) ρ_p - ρ_{env}, (f) $T_p < T_{env}$ and (g) $S_p <$

S_{env} for march 15, 2015. The dashback line denotes the depth of neutral buoyancy between the plume and the environment ($\rho_p = \rho_{env}$).

3.1.2 Shallow-diurnal convection

The shallow convective depths (<100m) observed in the tropics (30°S-30°N; Fig. 1a-h) are consistent with previous observations. Using the TAO mooring array across the tropical Pacific, Masich et al (2021) reported mean convective depths between 10 and 60 m. Using turbulence measurements from the TAO mooring at 0°,140°W, Moum et al. (2023) reported convective depths up to 90 m. In the tropical Atlantic, the same authors reported maximum convective depths of 65 m at 0°,23°W and 36 m at 0°,10°W, based on PIRATA mooring data, also consistent with our findings.

Hourly time series of w_p at the mooring site located at 2°S, 140°W, within the equatorial Pacific band where diurnal shallow convection occurs (Fig. 1a-d), are analyzed for July 2017 (Fig. 3a). Each night, convective plumes with w_p reaching up to 3.4 cm s^{-1} develop under surface buoyancy losses (~ –100 to –200 W m^{-2}), extending to depths between 50 and 100 m. The plumes exhibit a distinct asymmetry characterized by a prolonged deepening phase. For instance, on July 12, 2017, convection initiated around 8 p.m. with a shallow (< 10 m, Fig. 3b-f) and weak plume (~ 0.3 cm s^{-1}, Fig. 3b). As the night progressed, the plume deepened (to ~ 90 m) and intensified (to ~ 3 cm s^{-1}) for about 12 hours, peaking at 8 a.m (Fig. 3b). Following the gradual transition of the surface heat flux from negative to positive values, the plume weakened and eventually stopped at noon.

Due to localized instabilities along the density gradient, the MF component can occasionally be activated at depths, as observed on July 18 2017 at ~90 m depth (Fig. 3a). In this case, convection remains weak (w_p <0.5 cm s^{-1}) and confined to the neighboring grid cell. This behavior, here due to a local instability, indicates that the EDMF scheme is potentially capable of representing segmented convection not connected to the surface.

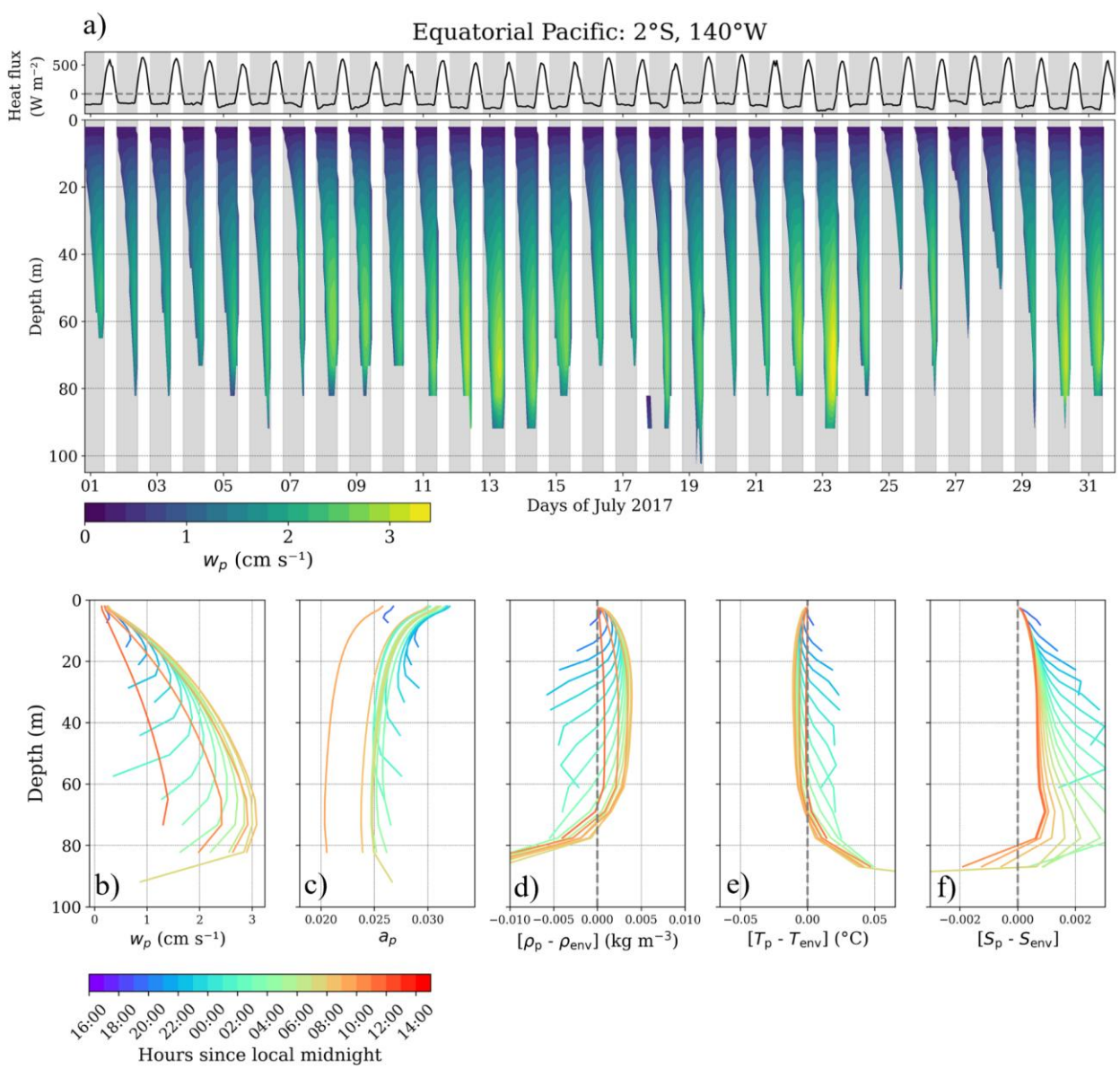


Figure 3: (a) Hourly time series of heat flux (W m^{-2}) and plume w_p (cm s^{-1}) for July 2017 at mooring location 2°S, 140°W in the Equatorial Pacific. 24-hours profiles of (b) w_p, (c) a_p, (d) ρ_p - ρ_{env}, (e) $T_p < T_{env}$ and (f) $S_p < S_{env}$ for july 13, 2017.

The modelled hourly temperatures at 2°S, 140°W are further compared to temperature observations from the TAO mooring for the period February 2017 to June 2018 (515 days), during which enhanced vertical resolution of temperature measurements was available (see Section 2.3). The data are sorted according to the observed daily mean wind speed (Fig. 4a). Days falling within the lowest 10% (lower decile) of wind speeds are classified as “low wind” conditions, while those in the highest 10% (higher decile) are classified as “high wind” conditions. The remaining 80% (interdecile) are classified as “medium wind” conditions. For each wind category, we construct daily composites of the temporal temperature gradient (°C/h).

For the period considered, observed cold plume penetration depths increase with wind intensity, from approximately 20 m under low wind conditions to ~60 m under high wind conditions, consistent with the findings of Masich et al. (2021) (Fig. 4b–d). This deepening is reproduced by all three simulations, with EDMF

simulation providing the best agreement with observations. In contrast, the TKE+EVD and TKE+MLP+EVD simulations tend to underestimate the cold plume penetration by ~10 to 20 m.

Additionally, the shape of the cold plumes in the EDMF simulation closely matches observations: cold anomalies continue to propagate for about one hour after the end of surface cooling, showing that the convective adjustment of water masses is not instantaneous but spreads over a time scale proportional to w_p/h where h is the depth of the unstable water column. In contrast, in the TKE+EVD and TKE+MLP+EVD simulations, cold anomalies cease at depth synchronously with the end of surface cooling. These results highlight the improved representation of shallow diurnal convection processes as a penetrative process by the EDMF parameterization in tropical regions. It should be noted that ad-hoc MLP and EVD modifications aimed at improving the TKE parameterization are now replaced by physical processes in EDMF.

The composites of the observations exhibit alternating patterns of positive and negative temperature anomalies below the plumes (Fig. 4c), potentially indicative of explicit tides that are not represented in the simulations.

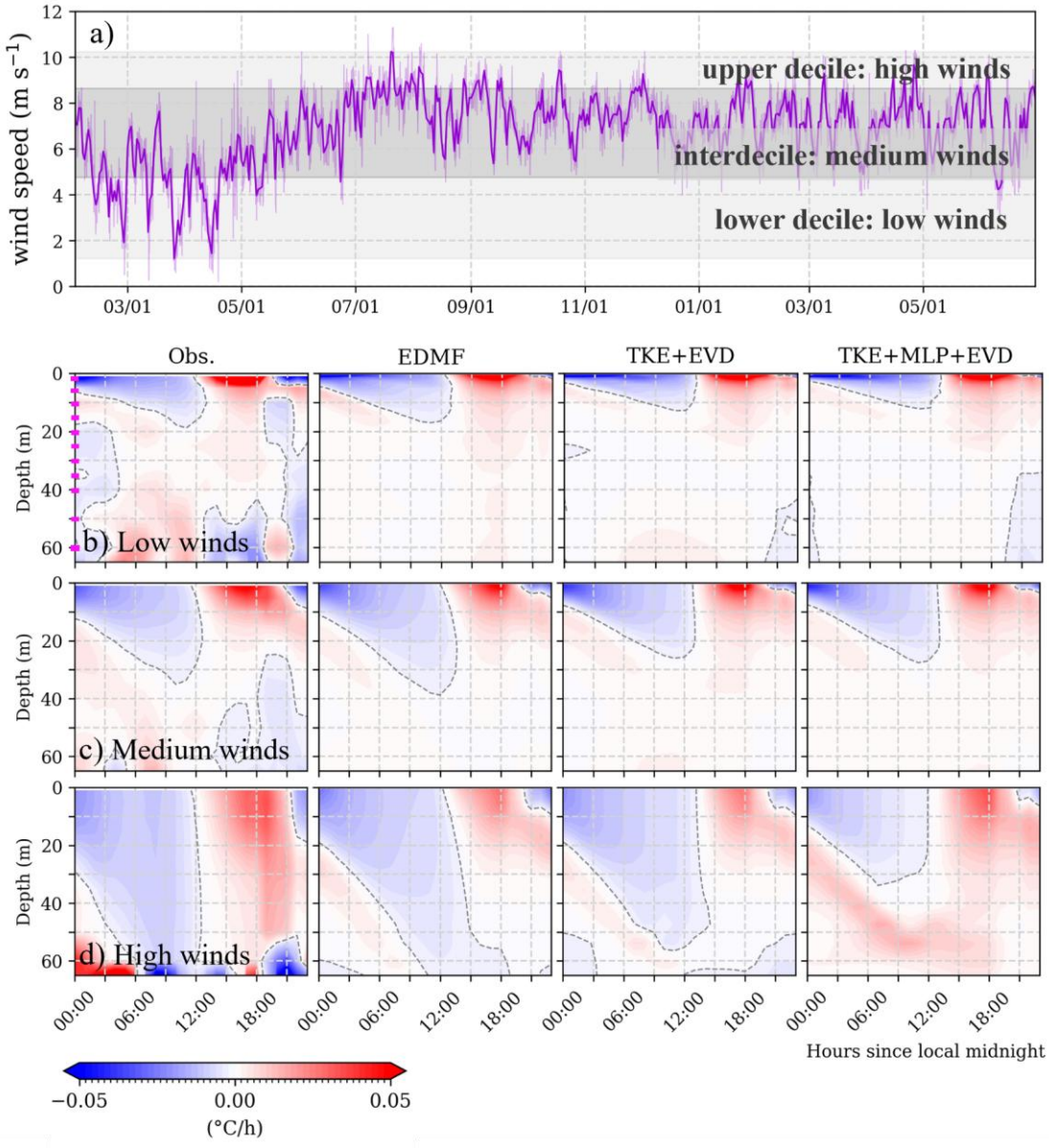


Figure 4 :(a) Wind speed at the TAO mooring located at 2°S, 140°W from February 2017 to June 2018, shown at an hourly (light purple) and at a daily resolution (dark purple). (b–d) Diurnal composites of the temporal gradient of temperature °C/h for observations (left column), the TKE+EDMF simulation (middle column), and the TKE+MLP+EVD simulation (right column), categorized by wind speed regimes: (b) lower decile [1.22–4.76 m s^{-1}], (c) interdecile range [4.77–8.63 m s^{-1}], and (d) upper decile [8.64–10.25 m s^{-1}]. Green squares in panel (b) indicate the depths of available in situ observations.

3.2 Global temperature patterns

This section focuses on the temperature of upper ocean layer (0–700 m), which accounts for approximately 60% of ocean heat uptake over the period 1970–2010 (Cheng et al., 2016) and contains the majority of observational data. Complementary analyses over the full 0–2000 m depth range, and for the salinity, are provided in the Supporting Information.

Figure 5 presents globally and regionally averaged temperature bias to temperature observations and root mean square deviation (RMSD) profiles in the upper ocean (0–700 m) for the three simulations. Additionally, Figure 6a–d shows annual averages of depth-averaged (0–700 m) temperature biases over the simulation period for each ocean basin.

At the global scale, the EDMF simulation displays lower 0-700 m depth-averaged temperature bias and RMSD compared to the TKE+MLP+EVD simulation, with averaged values over the simulation period of 0.152 and 0.211°C, respectively, corresponding to a global bias reduction of ~ 30% (Fig. 5a,b, Fig. 6a). Although the TKE+EVD simulation achieves the smallest global depth-averaged bias (0.05°C; Fig. 5a; Fig. 6a), this results from the compensation of a pronounced cold bias in the upper 0–100 m with a warm bias at greater depths (Fig. 5a). Considering the 0-2000 m depth range, EDMF simulation reduces the global temperature bias by ~ 80% compared to TKE+MLP+EVD simulation (Fig. S2a).

Across all three ocean basins considered, the EDMF simulation consistently produced the lowest depth-averaged bias compared to TKE+MLP+EVD simulation (Fig. 5b,e,g; Fig. 6b,c,d; Fig. S2), highlighting the scheme's improved capability in reproducing vertical temperature structures relative to the state-of-the-art simulation. In the tropical ocean, TKE+EVD and TKE+MLP+EVD present similar cold bias structures, though the addition of the MLP parameterization reduces the upper 300 m cold bias by ~ 0.25 °C in TKE+MLP+EVD (Fig. 5c), leading to a progressive cold bias reduction over time (Fig. 6b). A cold bias peak is observed at ~ 50 m for both TKE+EVD and TKE+MLP+EVD simulations. In contrast, the EDMF simulation exhibits distinct bias structures, transitioning from a surface cold bias to a warm bias between 100 and 200 m depth (Fig. 5c), which also contributes to a decrease of the tropical cold bias over time (Fig. 6b).

In both the northern and southern oceans, TKE+EVD and EDMF simulations exhibit similar vertical bias structures, characterized by alternating warm-cold-warm anomalies with increasing depth (Fig. 5e,g). In contrast, the TKE+MLP+EVD simulation displays a predominantly warm bias throughout the water column (Fig. 5e,g), resulting in higher depth-averaged warm biases over time (Fig. 6c,d). In the 150–700 m depth range of the southern ocean, both TKE+EVD and EDMF simulations substantially reduce the warm bias observed in TKE+MLP+EVD, with EDMF achieving the largest reduction (up to 0.4 °C, Fig. 5g) and the lowest depth-averaged warm biases over time (Fig. 6d).

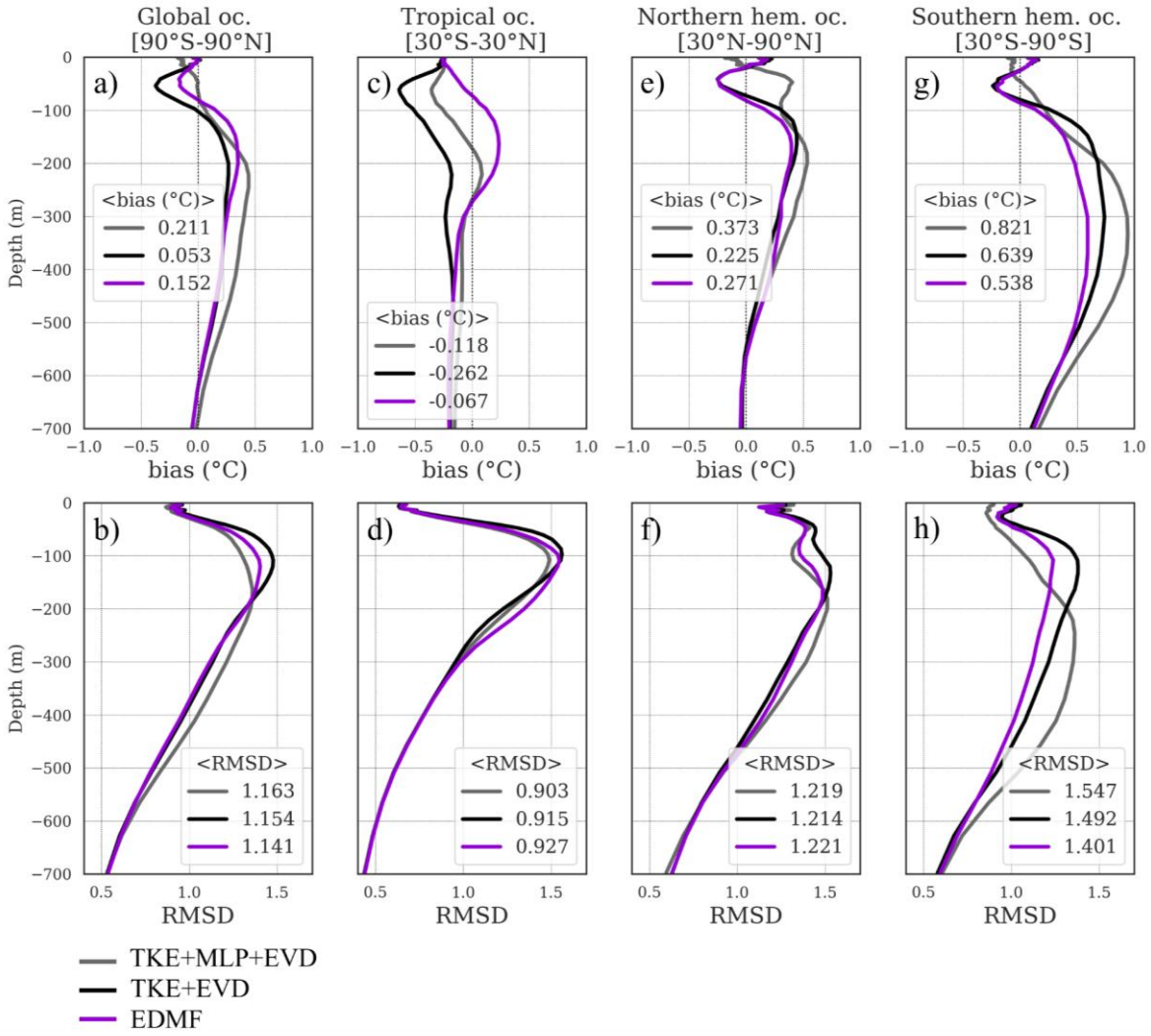


Figure 5: 0 to 700-m depth profiles of temperature bias (difference between the simulation and the observation; top row) and corresponding RMSD (bottom row) for the three simulations, averaged over the 2005-2020 period for the global ocean (a,b), for the tropical ocean (c,d), for the northern hemisphere ocean (e,f) and for the southern hemisphere ocean (g,h). 0 -700 m depth-averaged values of bias and RMSD are provided for each profile in the corresponding legend box.

The global interannual variability of observed upper-ocean temperature anomalies (relative to the 2005–2020 mean), characterized by a cooling phase during 2007-2011 followed by a warming phase from 2014 onward, is reproduced by all three simulations, although some discrepancies between the simulations exist (Fig. 6e,i,m,q). For example, the simulations underestimate the global warm anomalies observed throughout the water column in 2005-2006 (Fig. 6i,m,q). The underestimation is most pronounced in the TKE+MLP+EVD simulation, which produces cold anomalies between 200 and 600 m depth (Fig. 6q). This bias primarily originates in the southern ocean, where all three simulations show cold anomalies in this depth range in 2005-06, that are not supported by observations; the TKE+MLP+EVD simulation exhibits the strongest colder anomalies (Fig. 6h,l,p,t). In the

tropical ocean, all simulations overestimate the warm anomalies observed from 2005 to 2012 between ~200 to ~500 m depth, with TKE+EVD exhibiting warmest anomalies (Fig. 6f,j,n,r). From 2018 onward, the TKE+MLP+EVD fails at representing the observed vertical extent of the cold anomalies, which spread from ~ 100 to 700 m depth (Fig. 6f,r), while EDMF best represents these cold anomalies in terms of both depths and intensities (Fig. 6f,j).

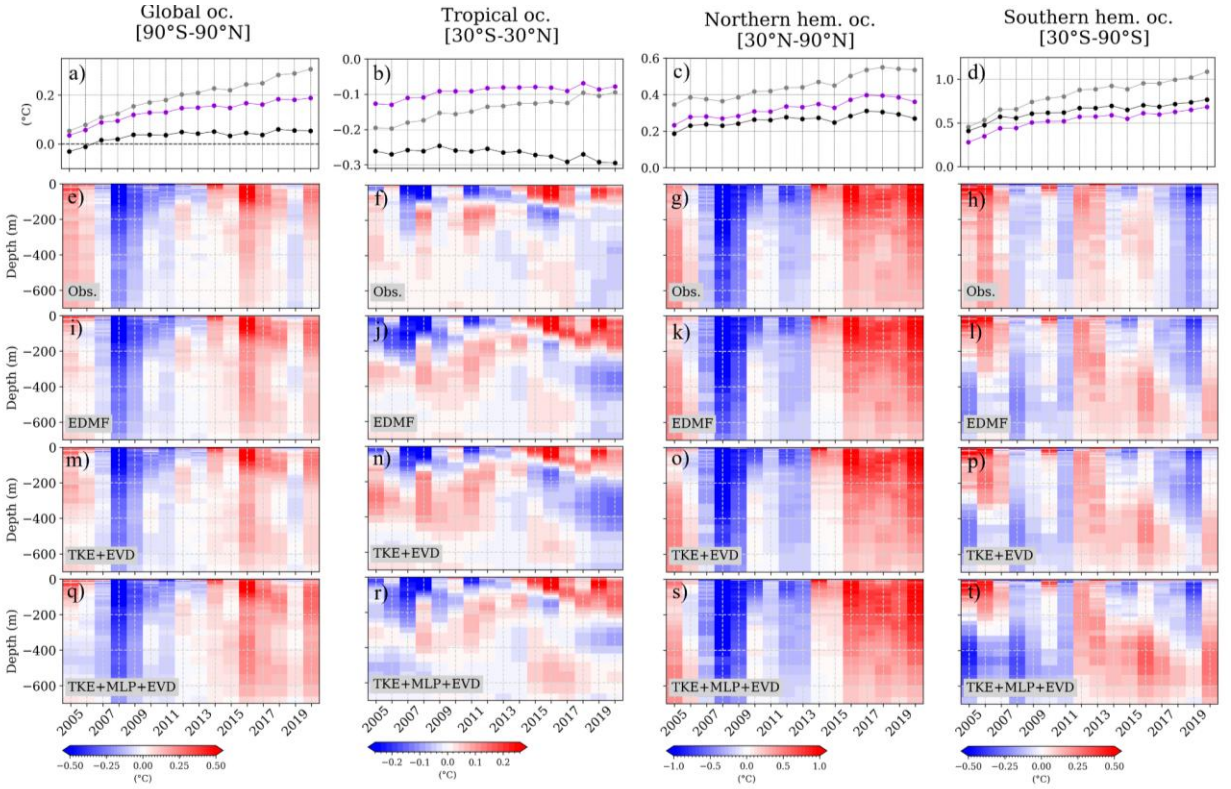


Figure 6: Observed and modelled annually-averaged temperature anomalies (°C) from 0 to 700 m depth, computed relative to the 2005-2020 mean, for (first column) the global ocean, (second column) the tropical ocean, (third column) the Northern Hemisphere ocean, and (fourth column) the Southern Hemisphere ocean. Panels (a–d) show the depth-averaged (0–700 m) temperature bias to observations time series for each region.

The performance of the EDMF and TKE+MLP+EVD simulations in representing the 0–700 m temperature fields averaged over the simulation period is further analyzed in Fig. 7. Complementary results for the 700–2000 m depth range are provided in Fig. S4, and for TKE+EVD simulation in Fig. S5.

Both simulations exhibit similar large-scale patterns of temperature bias in the 0-700 depth layer, characterized by cold anomalies across the tropical oceans and warm anomalies at high latitudes (Fig. 7c,g). Compared to TKE+MLP+EVD, the EDMF simulation generally reduces the 0–700 m temperature bias by ~0.5–1°C on a basin-wide scale, except in the tropical Atlantic and Indian Oceans, where EDMF shows slightly warmer anomalies (~0.2°C) than TKE+MLP+EVD (Fig. 7k).

As expected from Fig. 5, the influence of the mixing parameterization is limited at the surface and becomes more pronounced at depths (Fig. 7a,e,b,f). At the surface, sea surface temperature (SST) bias fields are similar between the two simulations, characterized by widespread cold anomalies across much of the global ocean (Fig. 7a,e). Exceptions include the western boundary current regions (Gulf Stream and Kuroshio), equatorial upwelling zones off Peru and Benguela, and the southern Pacific Ocean, where both simulations show warm

biases. These regional SST warm biases are consistent with previously reported radiation forcing errors in state-of-the-art climate models, particularly in the representation of longwave and shortwave fluxes due to a misrepresentation of low-level clouds (Zhang et al. 2023). Furthermore, western boundary currents are strongly affected by horizontal processes, including mesoscale eddies, fronts, and lateral advection, which are not fully resolved at the 1/4° horizontal resolution of our simulations. Consequently, these warm anomalies do not necessarily indicate a deficiency of the vertical mixing schemes, as they may partly reflect errors in the representation of horizontal dynamics and air–sea interactions.

At 100-m depth, the temperature bias fields of the two simulations (Fig. 7b,f) resemble those of the 0-700 m depth layer (Fig. 7c,g), although regional discrepancies emerge. For instance, the EDMF simulation exhibits a warmer bias of up to 1.5°C compared to TKE+MLP+EVD in the equatorial upwelling zones (Fig. 7b,f,j). In this case, night-time convection propagates warm waters to depth which mitigates the effects of the upwelling. Conversely, TKE+MLP+EVD exhibits colder anomalies by ~1°C in most of the tropical Pacific, confirming that the diurnal convection simulated by EDMF mitigates this cold bias because convection propagates warm water from the upper-layers downwards.

In the 700–2000 m depth layer, the patterns and intensities of the temperature bias and corresponding RMSD are similar between the two simulations, with basin-wide bias differences below 0.4 °C (Fig. S4). This result highlights the limited influence of the OBL parameterization in this depth range, where modifications to the temperature pattern occur over much longer timescales.

The tropical cold biases in the 0–700 m depth layer are more pronounced in the TKE+EVD simulation (Fig. S5g) compared to both EDMF and TKE+MLP+EVD simulations (Fig. 7c,g). This confirms that the EVD scheme alone is insufficient to accurately reproduce temperature values in this region (Fig. S5k). The enhanced cold anomalies in TKE+EVD extend towards the mid-latitudes of the southern ocean (20°S–40°S), which compensate for the warm biases observed in the two other simulations in this region (Fig. S5f,g,j,k; Fig. 7). Interestingly, opposite patterns are observed in the high latitudes where the warm biases at depths are enhanced in TKE+EVD (Fig. S5f) compared to EDMF and TKE+MLP+EVD simulations (Fig. 7b,f). In this case again, the EVD scheme alone fails at representing the observed temperature patterns.

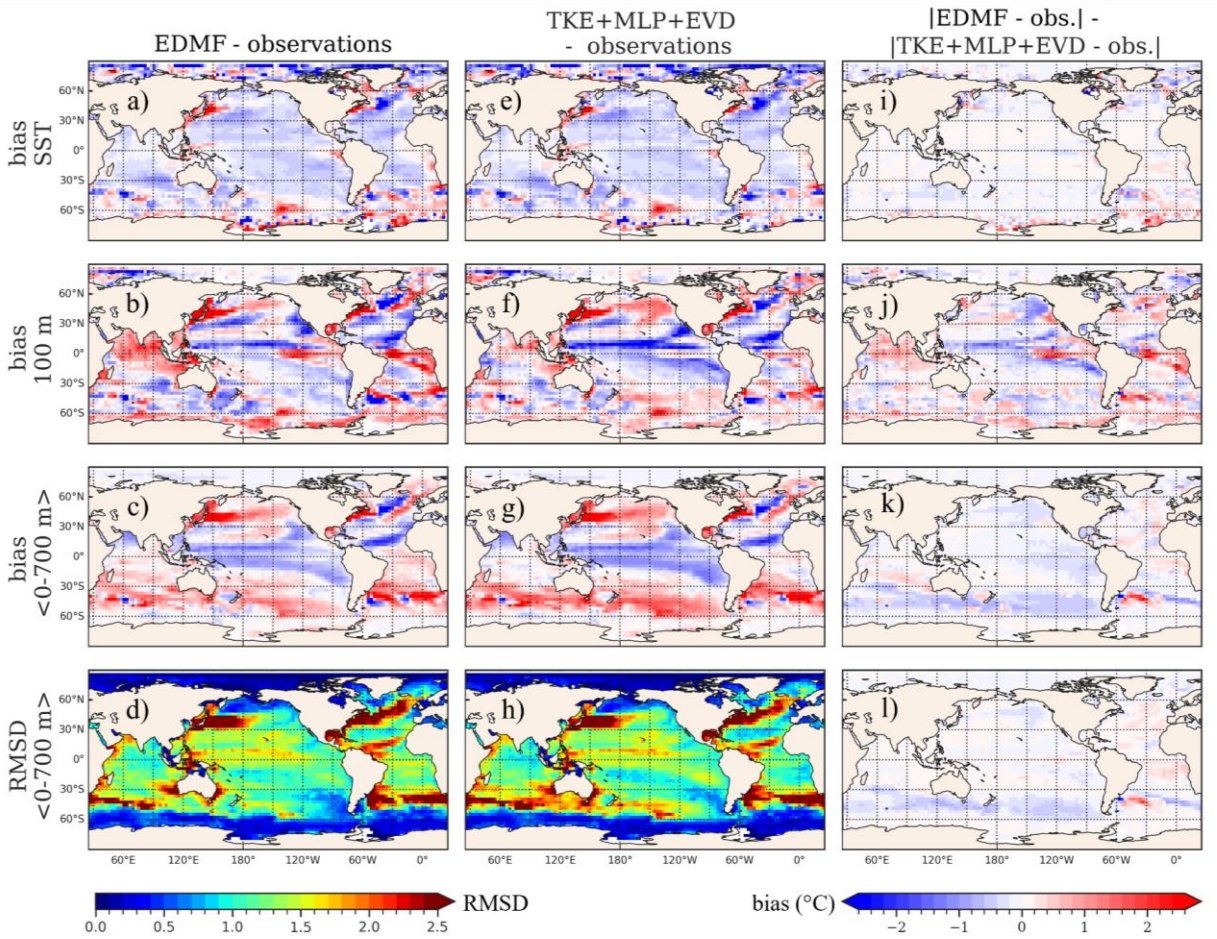


Figure 7: (a-d) Maps of bias between the EDMF simulation and the observations for SST (first row), temperature at 100 m (second row), depth-averaged temperature between 0 and 700 m (third row) and the corresponding 0-700 m averaged RMSD (fourth line). (e-h) Same as (a-d) but for the TKE+MLP+EVD simulation. (i-k) Maps of absolute differences between the biases for the three depth ranges considered, and (l) the corresponding RMSD differences.

3.3 Mixed-layer depth (MLD)

The global modeled seasonal cycle of MLD from both the EDMF and TKE+MLP+EVD simulations is close to the observed MLD throughout the year, although it is slightly deeper by ~5 m during JJAS and shallower by ~5 m during the rest of the year (Fig. 8a). In the tropical ocean, the EDMF simulation produces a seasonal MLD cycle that is closest to observations, while the other two simulations underestimate the observed cycles throughout the year (Fig. 8b).

In both the northern and southern hemisphere oceans, all simulations underestimate the observed monthly MLD during boreal and austral summers, respectively (Fig. 8c,d). During winter periods, the EDMF simulation produces deeper MLDs than the two EVD simulations in both extratropical oceans (Fig.8 c,d). This results in deeper-than-observed MLDs in the northern hemisphere ocean (Fig. 8c), while EDMF MLD is in close alignment with the observations in the southern hemisphere ocean (Fig.8d).

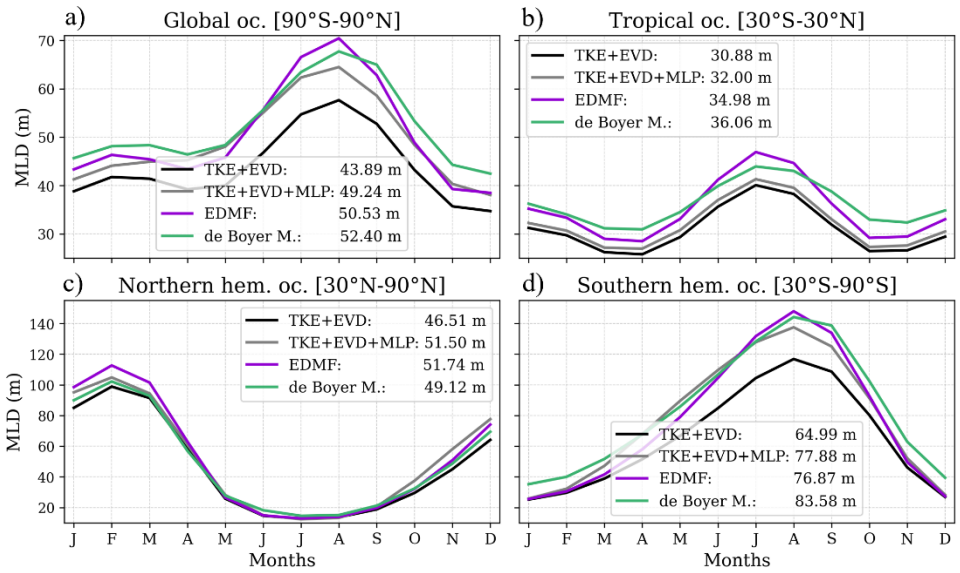


Figure 8: Seasonal cycle of MLD (in m) from the three simulations and the de Boyer Montégut (2024) dataset in the global (a), tropical (b), northern hemisphere (c) and southern hemisphere (d) ocean. Mean MLD values for each dataset are indicated within each panel.

The deeper monthly MLDs observed for EDMF in the northern hemisphere ocean originate from the deep convective regions of the Northern Atlantic ocean (Labrador, Irminger and Norwegian Sea), where MLDs from EDMF exceed those of TKE+MLP+EVD by up to 300 m during the January–February–March (JFM) period (Fig. 9a,b,e). In the rest of the northern hemisphere ocean, the MLDs from TKE+MLP+EVD are ~30 m deeper than those from EDMF (Fig. 9a). An opposite pattern is observed when comparing EDMF and TKE+EVD simulations during JFM (Fig. 9c,d,e). In most of the northern hemisphere ocean, EDMF produces MLDs that are ~ 20 to 50 m deeper than those from TKE+EVD (Fig. 9c). However, in the Labrador Sea, TKE+EVD generates JFM-averaged MLDs from 100 to 300 m deeper than those produced by EDMF (Fig. 9d,e).

To explain the discrepancies in MLDs among the simulations in the Labrador Sea, we investigate the temperature, salinity, density and Brunt–Väisälä frequency (N^2) profiles from the three simulations, both prior to and during the deep convection periods in winters 2011-12 and 2014-15 (Fig. 9f). Before the onset of the deep convection period, the TKE+MLP+EVD simulation exhibits deeper and weaker density gradients than those found in the TKE+EVD simulation, resulting in deeper MLDs in TKE+MLP+EVD by several tenth of meters. Correspondingly, the stratification levels in TKE+MLP+EVD, as indicated by N^2 values (~1×10^{-4} s^{-2}), are lower than those in TKE+EVD (>2.5×10^{-4} s^{-2}). This difference arises from the MLP parameterization, which enhances mixing in the thermocline year-round, especially at high latitudes (see section 2.1). The enhanced mixing erodes the vertical temperature gradients, thereby reducing the potential energy barrier that resists overturning.

Consequently, one would expect the weaker preconditioning stratification in TKE+MLP+EVD to favor deeper convection and MLDs than in TKE+EVD during the buoyancy loss period. However, the opposite occurs: the

MLP parameterization suppresses residual instabilities in the mixed layer, thereby reducing the frequency of EVD activations.

As a result, MLDs during convection periods are shallower in TKE+MLP+EVD by up to ~150 and ~600 m compared to TKE+EVD in winter 2011-12 and 2014-15, respectively. This highlights the regulation of the mixing by EVD through the MLP parameterization.

The stratification depths and intensities prior to the onset of the deep convection are similar between EDMF and TKE+EVD simulations (Fig. 9f,g), but the MLDs during the convection period differ between the two. In 2014-15 before the convection period, the water column is highly stratified for both EDMF and TKE+EVD ($N^2 > 3 \times 10^{-4}$ s^{-2}). Under intense surface buoyancy loss, the large mixing coefficient values assigned in TKE+EVD simulation is more efficient to erode the thermocline stratification than the convective velocities in EDMF simulation, resulting in shallower MLDs by ~ 200 in EDMF simulation.

With mild stratification conditions for both EDMF and TKE+EVD simulations ($2.2 < N^2 < 2.8 \times 10^{-4}$ s^{-2}) in the preconditioning period of 2011-12, the mixing coefficient values assigned in TKE+EVD produced MLDs that are ~ 50 m shallower than those of EDMF, because of limited residual instabilities and thus limited occurrences of EVD activations. This result is consistent with weaker surface buoyancy loss in 2011-12 than in 2014-15 (Fig. 9e).

Note that, although Argo-based MLD estimates are available for the Labrador Sea (e.g., Holte et al., 2017), a direct comparison with the box-averaged MLD shown here would require accounting for the heterogeneous spatial and temporal sampling of Argo profiles and applying consistent MLD diagnostics to the model profiles. Such a model–observation comparison is beyond the scope of the present study.

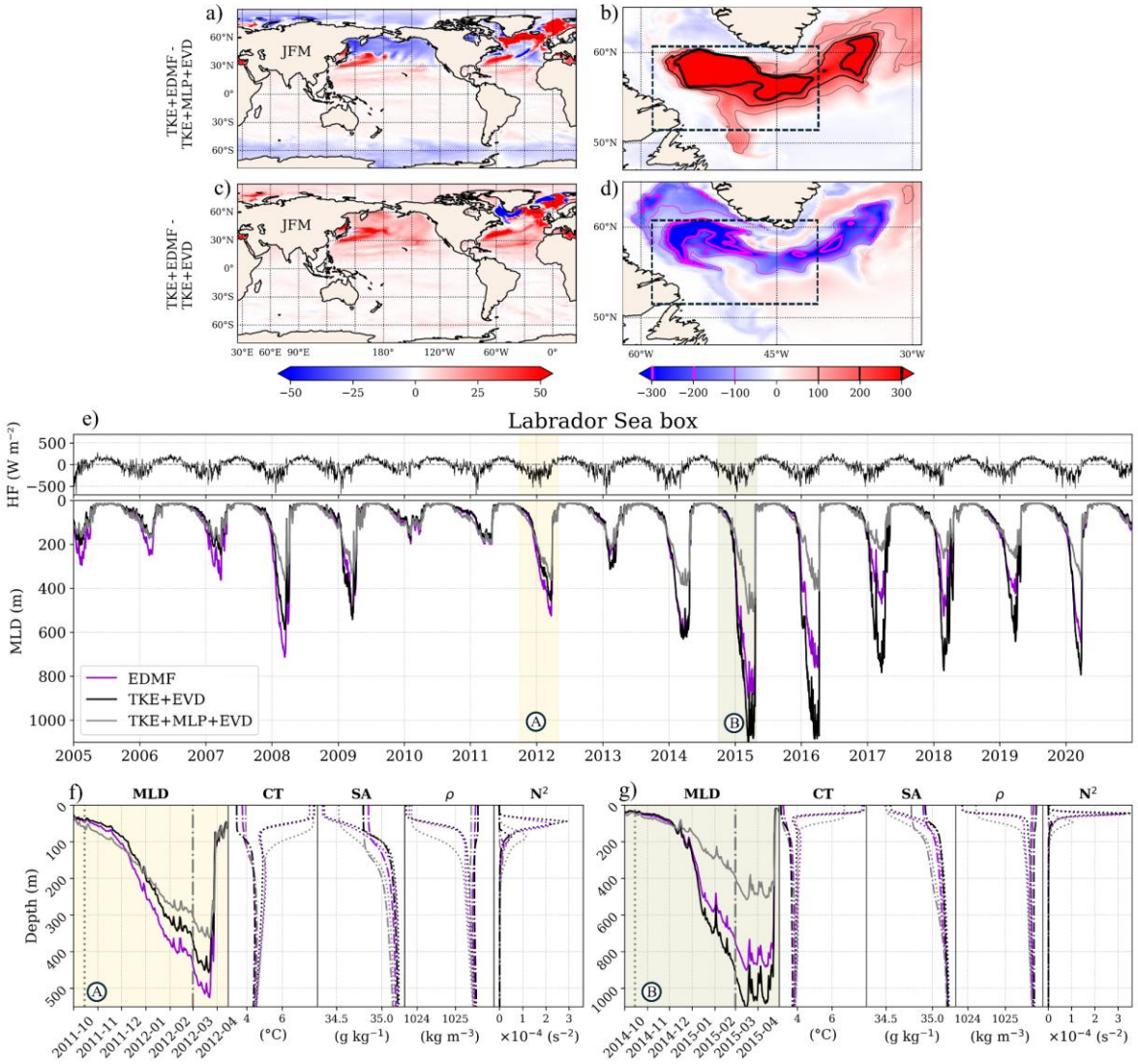


Figure 9: (a–d) Maps of mixed layer depth (MLD) differences (in m) computed for the JFM period between the EDMF simulation and (a,b) the TKE+MLP+EVD, and (c,d) the TKE+EVD simulations. (e) Time series of surface heat flux (W m^{-2}) and MLD (m) for the three simulations, averaged over the dashed black box representing the Labrador Sea shown in b,d. (f) MLDs during period A, along with vertical profiles of conservative temperature (CT, °C), absolute salinity (SA, g kg^{-1}), density (ρ, kg m^{-3}) and N^2 (s^{-2}) for selected days prior to (dotted lines) and during (dashed-dotted lines) the deep convection period, shown for all three simulations. (g) same as (f) but for period B.

4 Surface heat fluxes adjustments to EDMF

To assess how the mass-flux term affects surface heat fluxes, we analyze the seasonal variability of the fluxes component between the EDMF and TKE+EVD simulations. The analysis is carried out for the climatological seasons of JFM (January-February-March) and JAS (July-August-September) over several oceanic regions.

For both simulations, the heat accumulated over time in the surface layer at $z = 0$ (in K), is derived from the net surface heat flux that can be expressed as :

$$E(0,t) = \sum_{i=1}^{t} \frac{Q_{\mathrm{net}}(i)\, e_1\, e_2\, t_{\mathrm{mask}}(z)\, \Delta t}{V \rho_0\, C_p} = \sum_{i=1}^{t} F(0) \Delta t \tag{8}$$

where $Qnet$ is the net downward air-sea heat flux (W m^{-2}), ρ_0 is the density of seawater at the surface (kg m^{-3}), C_p is the specific heat capacity of seawater (J kg^{-1} K^{-1}), Δt the elapsed time (in s), and V is the total ocean volume (in m^3).

The air-sea heat flux (Q_{net}) is decomposed as:

$$Q\mathrm{net} = SW\mathrm{net} + LW\mathrm{net} + SH + LH, \tag{9}$$

$$\text{where } SW\mathrm{net} = SW_{\downarrow} - SW_{\uparrow} \text{ and } LW\mathrm{net} = LW_{\downarrow} - LW_{\uparrow}, \tag{10}$$

with $SW\mathrm{net}$ the net shortwave radiation flux, $LW\mathrm{net}$ the net longwave radiation flux, SH the sensible heat flux and LH the latent heat flux.

The bulk formulae of the ocean model provide SH and LH. As the downward longwave flux $LW_{\downarrow}$ and $SW_{\downarrow}$ are prescribed from the ERA5 reanalysis and are common to the two simulations, the $LW_{\uparrow}$ and $SW_{\uparrow}$ are diagnosed for each simulation from Eq. 10.

In that way the simulated global ocean mean temperature (in K) change is expressed as:

$$\delta T(t) = T(t) - T(0) = E(0,t), \text{ with} \tag{11}$$

$$T(t) = \sum_{z=0}^{z=h} \frac{T(z,t)\, e_1 e_2\, t_{\mathrm{mask}}(z)\, e_3(z)}{V} \tag{12}$$

where h is the bottom vertical level and e1, e2, e3 the scaling factors. This means that $\delta T(t)$ is controlled solely by the net surface heat forcing at global scale.

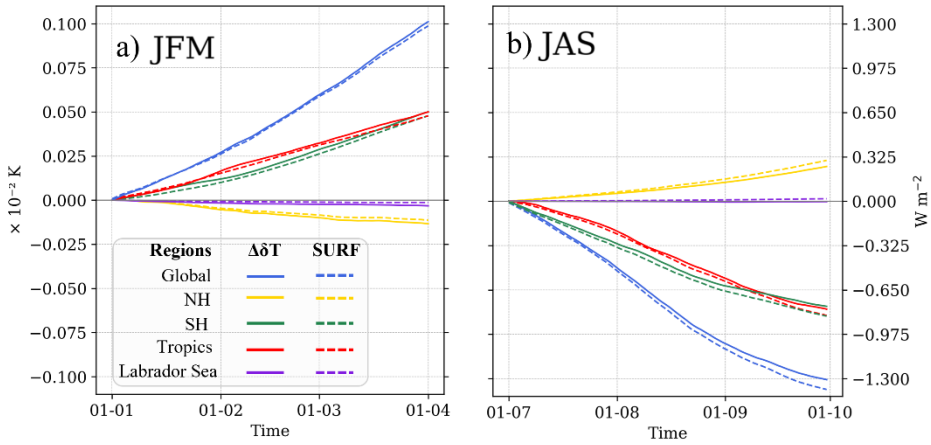
Therefore the variation in global temperature between the two simulations ($\Delta\delta T(t)$) is associated with the adjustment of the net surface heat flux (SURF) induced by the change in vertical scheme.

$$\Delta\delta T(t) = \delta T_{\mathrm{EDMF}}(t) - \delta T_{\mathrm{TKE+EVD}}(t) = SURF$$

and the components of SURF are expressed as:

$$\Delta SW\mathrm{net} = SW\mathrm{net}_{EDMF}(0,t) - SW\mathrm{net}_{TKE+EVD}(0,t),$$
$$\Delta LW_{\uparrow} = LW_{\uparrow}{}_{EDMF}(0,t) - LW_{\uparrow}{}_{TKE+EVD}(0,t),$$

$$\Delta SH = SH_{EDMF}(0,t) - SH_{TKE+EVD}(0,t) \text{ and}$$
$$\Delta LH = LH_{EDMF}(0,t) - LH_{TKE+EVD}(0,t). \quad (13)$$



× 10⁻² K
W m⁻²

c) JFM

	Δ(Tair − SST)	SURF	ΔSW	ΔLW ↑	ΔLH	ΔSH
Global	3.57 *46.4*	3.82 *49.7*	-0.09 *-1.17*	0.45 *5.85*	2.38 *30.9*	1.09 *14.17*
NH	-0.26 *-3.38*	-0.12 *-1.56*	0.02 *0.26*	-0.02 *-0.26*	-0.06 *-0.78*	-0.05 *-0.65*
SH	2.38 *29.6*	1.84 *23.9*	-0.11 *-1.43*	0.26 *3.38*	1.00 *13.0*	0.68 *8.84*
Tropics	1.45 *18.9*	2.10 *27.3*	0.00 *0.00*	0.21 *2.73*	1.44 *18.7*	0.45 *5.85*
Labrador Sea	-0.03 *-0.39*	-0.07 *-0.91*	-0.00 *-0.00*	-0.01 *-0.13*	-0.03 *-0.39*	-0.03 *-0.39*

d) JAS

× 10⁻² K
W m⁻²

Global	-4.18 *-54.3*	-4.97 *-64.6*	0.01 *0.13*	-0.58 *-7.54*	-2.80 *-36.4*	-1.60 *-20.8*
NH	1.12 *14.6*	0.87 *11.3*	-0.03 *-0.39*	0.14 *1.82*	0.50 *6.50*	0.25 *3.25*
SH	-2.65 *-34.5*	-2.95 *-38.4*	0.03 *0.39*	-0.34 *-4.42*	-1.44 *-18.7*	-1.21 *-15.7*
Tropics	-2.64 *-34.3*	-2.89 *-37.6*	0.00 *0.00*	-0.37 *-4.81*	-1.87 *-24.3*	-0.65 *-8.45*
Labrador Sea	0.08 *1.04*	0.05 *0.65*	-0.00 *-0.00*	0.01 *0.13*	0.02 *0.26*	0.02 *0.26*

Δ(Tair – SST) = (Tair – SST_{EDMF}) - (Tair – SST_{EVD})
SURF = E_{EDMF} – E_{EVD}
ΔSW = $SWnet_{EDMF}$ – $SWnet_{EVD}$
ΔLW = $LW\uparrow_{EDMF}$ – $LW\uparrow_{EVD}$
ΔLH = LH_{EDMF} – LH_{EVD}
ΔSH = SH_{EDMF} – SH_{EVD}

−1.00 −0.75 −0.50 −0.25 0.00 0.25 0.50 0.75 1.00
Normalized contribution to SURF

Figure 10: Time series of SURF (10^{-2} K on the left y-axis; W m^{-2} on the right y-axis) for the climatological seasons of JFM (a) and JAS (b), computed for the global, northern hemisphere (NH), southern hemisphere (SH), tropical oceans and the Labrador Sea. Corresponding cumulative values of SURF, ΔSW, $\Delta LW_{\uparrow}$, ΔLH, ΔSH, expressed in 10^{-2} K and in W m^{-2} (in italics) for JFM (c) and JAS (d). The sign convention of these values is given in Eq. 13. The colorbar indicates the normalized contribution of each heat flux component to SURF.

The $\Delta\delta T(t)$ and SURF time series (Fig. 10a,b) show high consistency at global and seasonal scales. At the end of the period, the cumulative surface fluxes do not deviate by more than 3% from the temperature variations, which indicate a good closure of the global heat budget.

In the global ocean, the $\delta\Delta T(t)$ and SURF timeseries exhibit opposite behaviors between the JFM and JAS seasons, with increasing positive values in JFM and decreasing negative values in JAS (Fig. 10a,b). Positive SURF values indicate that the net surface heat loss in EDMF simulation is less than in TKE+EVD simulation. The higher component of SURF in EDMF arises primarily (~59%) from reduced latent heat (LH) loss and secondarily (~27%) from reduced sensible heat (SH) loss relative to TKE+EVD (Fig. 10c). Because heat fluxes are defined as positive downwards, positive ΔLH and ΔSH correspond to weaker upward (negative) LH_{EDMF} and SH_{EDMF} compared to LH_{EVD} and SH_{EVD}. These reduced LH_{EDMF} and SH_{EDMF} values result from globally cooler SSTs in EDMF ($\Delta Tair - SST$ >0), which reduces the air–sea temperature and humidity gradients and thus the turbulent heat loss to the atmosphere.

The longwave upward radiative flux differences ($\Delta LW_{\uparrow}$) contribution to SURF is more moderate (~10%), reflecting slightly weaker infrared cooling in EDMF due to cooler SST. Shortwave fluxes differences (ΔSW) contribute only marginally to SURF (~2%) and originate from differences in $SW_{\uparrow}$, which are linked to regional differences in sea-ice concentration – most notably along the Greenland margins and in the Sea of Okhotsk (Fig. S7e, f). Similar contributions of ΔLH, ΔSH and $\Delta LW_{\uparrow}$ are found in the southern hemisphere and tropical oceans (Fig. 10c).

In the Northern Hemisphere ocean, the negative SURF values in JFM are again dominated by contributions from ΔLH, followed by ΔSH and $\Delta LW_{\uparrow}$ (Fig. 10a, c). Here, negative values indicate stronger upward LH_{EDMF}, SH_{EDMF} and $LW^{\uparrow}{}_{EDMF}$ relative to EVD. These enhanced turbulent and radiative losses arise from warmer SSTs in EDMF due to less turbulent entrainment at the mixed-layer base, which increase the air-sea temperature and humidity gradient and thus enhance heat loss to the atmosphere.

The Labrador Sea also exhibits negative SURF values in JFM – consistent with SURF in the northern hemisphere – but with comparable contributions from $\Delta LH$and ΔSH (Fig. 10a, c). In this region, extremely cold and dry winter conditions produce low near-surface humidity (q_a), while higher SSTs lead to higher specific humidity saturation ($q_{sat}(SST)$) in the EDMF simulation in accordance with the Clausius–Clapeyron relation. The SST adjustment and the Clausius-Clapeyron law control the turbulent heat flux sensitivity between the two simulations.

As expected from the seasonal transition, opposite patterns emerge during JAS, with negative SURF values in the global, southern hemisphere, and tropical oceans, and positive SURF values in the northern hemisphere ocean and Labrador Sea (Fig. 10b, d). This result stems from the fact that turbulent entrainment is more intense with EVD than with EDMF in JAS, i.e., during winter in the Southern Hemisphere, whereas it is the opposite in the northern hemisphere ocean, where the vertical mixing is more intense in summer with EDMF than with EVD. As in JFM, ΔLH remains the dominant contributor to SURF, followed by ΔSH and $LW_{\uparrow}$. An exception occurs again in the Labrador Sea where contributions of ΔLH and ΔSH are of similar magnitude.

The opposite adjustments of SURF and its individual components observed during the JAS season (Fig. 10b) are driven by positive SST anomalies induced by the EDMF scheme. These adjustments occur with proportions comparable to those diagnosed during the JFM season. At the global scale, the SURF signal is controlled by the Southern Hemisphere and the tropical oceans rather than by the Northern Hemisphere ocean, for both seasons. This reflects the larger oceanic surface area in the Southern Hemisphere, which dominates the global heat budget.

Consequently, the global positive (negative) SURF anomalies in JFM (JAS; Fig. 10a,b) are associated with negative (positive) SST anomalies, respectively. This result indicates that the entrainment at the base of the mixed layer is stronger (weaker) for EDMF than for EVD during JFM (JAS), i.e. in the summer hemisphere (winter) hemisphere, because the seasonal cycle is dominated by the Southern Hemisphere ocean. This result shows that the mixing process is more enhanced for EVD than for EDMF in winter and vice versa in summer. This global entrainment response, supported by the Southern Hemisphere and the tropical oceans, is partly offset by opposite SURF adjustments in the Northern Hemisphere ocean and Labrador Sea. In these regions, EDMF induces reduced vertical mixing during JFM and enhanced mixing during JAS, leading to negative and positive SURF anomalies, respectively. However, the contribution of the Northern Hemisphere ocean does not dominate the global signal. This response is consistent with the MLDs shown in Fig. 9e,f, particularly from 2015 onward, where the TKE+EVD simulation exhibits systematically deeper MLDs than EDMF. These deeper MLDs result from very frequent EVD activations, which lead to a significant deepening of the mixed layer.

The global temperature adjustment induced by the EDMF scheme results from adjustments in surface heat fluxes, and in decreasing order: ΔLH, ΔSH, $LW_{\uparrow}$. In terms of energy, this adjustment corresponds to an average amount of energy on the order of 10^7 J m^{-2}, estimated from $\Delta J = \rho_0 \, C_p \, H(=2500m) \, \Delta T(=0.001K)$, which represents 1.3 W m^{-2} on a seasonal timescale. This adjustment represents ~6.5% of the global net surface heat flux climatology (~20 W m^{-2}) proposed by Tomita et al. (2021). Such non-negligible adjustment suggests that the EDMF parameterization can substantially influence processes associated with water-mass formation such as modal water production, particularly in subpolar or subtropical regions. Consequently, the use of EDMF has the potential to improve physical realism of vertical mixing and surface-interior heat exchange, thereby contributing to more reliable climate simulations.

5 Discussion and Conclusion

This study presents the first global implementation and evaluation of the Eddy-Diffusivity Mass-Flux (EDMF) parameterization for oceanic convection within the NEMO framework. The EDMF approach has the advantage of describing in a unified way both diffusive (local) and non-diffusive (non-local) turbulent mixing that are the main mixing regimes of the ocean boundary layer (OBL), with numerics tailored to each process (Giordani et al. 2020). By explicitly representing the non-local transport associated with convective plumes, EDMF fundamentally departs from the Enhanced Vertical Diffusion (EVD) approach combined with the Mixed-Layer Penetration (MLP) parametrization that are traditionally used in NEMO, in which convection is represented through strong local diffusion. Our results reveal several key improvements associated with EDMF, in terms of

convective regimes, global upper-ocean temperature and mixed layer depth (MLD) compared to a state-of-the-art EVD+MLP approach.

Based on a 16-year simulation period, we show that EDMF, which uses a unique formulation, successfully captures the two distinct regimes of oceanic convection: shallow diurnal convection prevalent in the tropics, and deep wintertime convection occurring in subpolar regions.

In the tropics, EDMF closely reproduces the penetrative and temporally asymmetric behavior of shallow convection, including its persistence beyond the cessation of nighttime surface cooling. In comparison, EVD-based approaches fail to represent this persistence and they underestimated the plume penetration depths.

In the northern Atlantic subpolar region, EDMF reproduced the seasonality, depths and intensities of the observed convective plumes. In particular, the scheme captured the major deep convection event of winter 2014-15 that occurred in the Labrador and Irminger Seas. In comparison, the TKE+EVD+MLP simulation largely underestimated the MLDs during this event. As MLP weakens the stratification during the preconditioning period (autumn), the activations of EVD are less frequent, resulting in weak vertical mixing and shallow MLDs.

At the global scale, EDMF reduces the temperature biases by ~ 30% in the upper 700 m compared to the state-of-the-art TKE+MLP+EVD configuration. This improvement primarily stems from a more realistic representation of convection basin-wide, leading to improved representation of the vertical distribution of heat within the mixed layer and thus reduced warm biases in both hemispheres. In the tropics, the long-standing subsurface cold bias in EVD-based simulations is mitigated in EDMF as the scheme conveys warm waters from the upper-layers downwards. These reductions in temperature biases obtained with EDMF should nevertheless be interpreted with caution as they reflect the combined effect of EDMF, the other parameterizations, the surface forcing and their interactions. In particular, the present simulation was not accompanied by a re-tuning of other parameterizations following the implementation of EDMF, e.g. the eddy-induced velocities parameterization (Gent and McWilliams,1990), the submesoscale mixed layer eddies parameterization (Fox-Kemper et al. 2008), or the vertical TKE closure scheme. Further improvements in the global mean state of temperature may therefore be possible through a joint re-tuning of the model components. These results should thus be viewed as an indication of the beneficial impact of EDMF formulation, rather than as a standalone demonstration of improved physical realism.

The EDMF parameterization further modifies the oceanic heat balance by adjusting surface heat fluxes. This adjustment, primarily driven by latent heat flux, changes the net climatological surface heat balance by approximately 6-7%. This has consequences for the worldwide SST diurnal cycle and global subtropical mode waters, which are mainly produced in the Gulf Stream (Gan et al., 2023). In coupled ocean-atmosphere mode, adjustments to large-scale atmospheric circulation, surface fluxes and associated precipitation are also to be expected.

Overall, this global-scale assessment demonstrates the impact of introducing EDMF representation of local and non-local vertical mixing into a global ocean model. This study further illustrates that the EDMF parameterization is a credible alternative to the traditional TKE+EVD+MLP approach. EDMF eliminates the need for empirical adjustments such as MLP, offering a physically grounded alternative for mixed-layer

deepening processes. The overarching objective of EDMF is indeed to move away from the use of empirical adjustments such as EVD and MLP and towards a more physically-based representation of turbulent mixing at the base of the mixed-layer. We recognize that this is a challenging task, given that the NEMO configuration has been originally tuned around the existing EVD and MLP framework. In addition, convection interacts strongly with eddy-induced restratification processes. As a next step, we therefore plan to use the GEOMETRIC parameterization to represent sub-mesoscale restratification in NEMO. Consequently, future work will include parameters tuning to consider EDMF, GEOMETRIC, and other evolving parameterizations jointly rather than tuning each component independently.

For climate simulations, we plan to adjust the EDMF parameters, particularly those controlling lateral exchanges between convective plumes and their environment, using the High-Tune method (Couvreux et al., 2021). High-Tune provides a more rational semi-automatic calibration framework than empirical tuning, as it is designed to avoid over-calibration of parameters.

A remaining question is how convection interacts with double-diffusion mixing. This is an important issue, as both processes play key roles in the formation and transformation of water masses and contribute to the large-scale thermohaline circulation (Zhang and Schmitt, 1998). Their interaction therefore warrants further investigation.

Data Availibility Statement

All simulations presented in this paper are based on NEMO_release_4.2.2 and supplementary routines, input data and simulations outputs dedicated to convection are available on Mercator Ocean International ftp (ftp://ftp.mercator-ocean.fr/download/users/rbourdal/data_JAMES).

Author contributions

VP and RBB designed the methodology and the experiments, VP carried them out. VP carried the formal analysis. RBB, HG and CP developed the code. VP prepared the manuscript (original draft preparation) with contributions from all co-authors.

Competing interests

None

Acknowledgments

This work has received funding from the European Union's H2020 research and innovation program under grant agreement N. 101003536 (ESM2025 – Earth System Models for the Future). This study has received funding from Agence Nationale de la Recherche - France 2030 as part of the PEPR TRACCS program under grand number ANR-22-EXTR-0008.

References

Allende, S., A. M. Treguier, C. Lique, C. de Boyer Montégut, F. Massonnet, T. Fichefet, and A. Bathélémy. 2024. Impact of ocean vertical-mixing parameterization on Arctic sea ice and upper-ocean properties using the NEMO-SI3 model. Geosci. Model Dev. 17: 7445-7466. https://doi.org/10.5194/gmd-17-7445-2024

Bellenger, H., and J.-P. Duvel. 2009. An analysis of tropical ocean diurnal warm layers. J. Climate. 22: 3629-3646. https://doi.org/10.1175/2008jcli2598.1

Behrens, E., G. Rickard, O. Morgenstern, T. Martin, A. Osprey, and M. Joshi. 2016. Southern Ocean deep convection in global climate models: A driver for variability of subpolar gyres and Drake Passage transport on decadal timescales. J. Geophys. Res. Oc. 121: 3905–3925. https://doi.org/10.1002/2015JC011286

Blanke, B., and P. Delecluse. 1993. Variability of the tropical Atlantic Ocean simulated by a general circulation model with two different mixed-layer physics. J. Phys. Oceanogr. 23:1363-1388. https://doi.org/10.1175/1520-0485(1993)023<1363:VOTTAO>2.0.CO;2

de Boyer Montégut, C. 2024. Mixed layer depth over the global ocean : a climatology computed with a density threshold criterion of 0.03 kg/m3 from the value at the reference depth of 5 m. SEANOE. https://doi.org/10.17882/98226

de Boyer Montégut, C., G. Madec, S. Fischer Albert, A. Lazar, and D. Iudicone. 2004. Mixed layer depth over the global ocean: An examination of profile data and a profile-based climatology. J. Geophys Res. Oc. 109: 1-20. https://doi.org/10.1029/2004JC002378

Calvert, D., and J. Siddorn. 2013. Revised vertical mixing parameters for the UK community standard configuration of the global NEMO ocean model, Met Office Hadley Center Technical Note, 95, 207517, https://library.metoffice.gov.uk/Portal/Default/en-GB/RecordView/Index/207517 (last access: 1 April 2025)

Cheng, L., K. E. Trenberth, M. D. Palmer, J. Zhu, and J. P. Abraham. 2016. Observed and simulated full-depth ocean heat content changes for 1970-2005. Oc. Sci. 12: 925-93. https://doi.org/10.5194/os-12-925-2016

Couvreux, F., F. Hourdin, D. Williamson, R. Roehrig, V. Volodina, N. Villefranque, C. Rio, O. Ardouin, J. Salter, E. Bazile, F. Brient, F. Favot, R. Honnert, M.-P. Lefebvre, J.-B. Madeleine, Q. Rodier, and W. Xu. 2021. Process-based climate model development harnessing machine learning: I. A calibration tool for parameterization improvement. J. Adv. Model. Earth Sys. 13: e2020MS002217. https://doi.org/10.1029/2020MS002217

Fox-Kemper, B., A. Adcroft, C. W. Böning, E. P. Chassignet, E. Curchitser, G. Danabasoglu et al. 2019. Challenges and prospects in ocean circulation models. Front. Mar. Sci. 6: 65. https://doi.org/10.3389/fmars.2019.00065

Frajka-Williams, E., P. B. Rhines, and C. C. Eriksen. 2014.Horizontal stratification during deep convection in the Labrador Sea. J. Phys. Oceanogr. 44: 220-228. https://doi.org/10.1175/JPO-D-13-069.1

Gan, B., J. Yu, L. Wu, G. Danabasoglu, R. J. Small, A. H. Baker, F. Jia, Z. Jing, X. Ma, H. Yang, Z. Chen. 2023. North Atlantic subtropical mode water formation controlled by Gulf Stream fronts. Nat. Sci. Rev. 10: https://doi.org/10.1093/nsr/nwad133

Garanaik, A., F. S. Pereira, L. Smith, R. Robey, Q. Li, B. Pearson, and L. Van Roekel (2024) A new hybrid mass-flux/high-order turbulence closure for ocean vertical mixing. J. Adv. Model. Earth Sys. 16: e2023MS003846. https://doi.org/10.1029/2023MS003846

Gaspar, P., Y. Gregoris, and J. M. Lefevre. 1990. A simple eddy kinetic energy model for simulations of the oceanic vertical mixing: Tests at station Papa and long-term upper ocean study site. J. Geophys. Res. 95: 19179-16193: https://doi.org/10.1029/JC095iC09p16179

Giordani, H., R. Bourdallé-Badie, and G. Madec. 2020. An eddy-diffusivity mass-flux parameterization for modeling oceanic convection. J. Adv. Model. Earth Sci. 12: e2020MS002078. https://doi.org/10.1029/2020MS002078

Gordon A. L. 1978. Deep Antarctic convection west of Maud Rise. J. Phys. Oceanogr. 8: 600-612. https://doi.org/10.1175/1520-0485(1978)008<0600:DACWOM>2.0.CO;2

Gülk B. F. Roquet, A. C. Naveira Garabato, R. Bourdallé-Badie, G. Madec, and H. Giordani. 2024. Impacts of vertical convective mixing schemes and freshwater forcing on the 2016-2017 Maud Rise polynia openings in a regional ocean simulation. J. Adv. Model. Earth Sys. 13: e2023MS004106. https://doi.org/10.1029/2023MS004106

Herbasch et al. 2020. The ERA5 global reanalysis. Q. J. Roy. Meteor. Soc., 146, 1999–2049

Heuzé, C., J. K. Ridley, D. Calvert, D. P. Stevens, and K. J. Heywood. 2015. Increasing vertical mixing to reduce Southern Ocean deep convection in NEMO3.4. Geosci. Model Dev. 8:3119-3130. https://doi.org/10.5194/gmd-8-3119-2015

Holte, J., and L. D. Talley. 2009. A new algorithm for finding mixed layer depths with applications to Argo data and subantarctic mode water formation. J. Atmos. Oc. Tech. 26: 1920-1939. https://doi.org/10.1175/2009JTECHO543.1

Holte, J., L. D. Talley, J. Gilson, and D. Roemmich .2017. An Argo mixed layer climatology and database, Geophys. Res. Lett. 44: 5618–5626. https://doi.org/10.1002/2017GL073426

Houpert, L., X. Durrieu de Madron, P. Testor, A. Bosse, F. d'Ortenzio, M. N. Bouin, D. Dauss, H. Le Goff, S. Kunesch, M. Labast. et al. 2016. Observations of open-ocean deep convection in the northwestern Mediterranean Sea: Seasonal and interannual variability of mixing and deep water masses for the 2007-2013 period. J. Geophys. Res. Oc. 121: 8139-8171. https://doi.org/10.1002/2016JC011857

Hourdin, F., D. Williamson, C. Rio, F. Couvreux, R. Roehrig, N. Villefranque, I. Musat, L. Fairhead, F. Binta Diallo, and V. Volodina. 2021. Process-based climate model development harnessing machine learning: II. Model calibration from single column to global. J. Adv. Model. Earth Sys. 13: e2020MS002225 https://doi.org/10.1029/2020MS002225

Hourdin, F., B. Ferster, J. Deshayes, J. Mignot, I. Musat, and D. Williamson. 2023.Toward machine-assisted tuning avoiding the underestimation of climate change projections uncertainty. Sci. Adv. 9: eadf2758. doi: 10.1126/sciadv.adf2758

Kieke, D., and I. Yashayaev. 2015. Studies of Labrador Sea Water formation and variability in the subpolar North Atlantic in the light of international partnership and collaboration, Prog. Oceanogr. 132: 220–232. https://doi.org/10.1016/j.pocean.2014.12.010

Large, W. G., J. C. McWilliams, and S. C. Doney. 1994. Oceanic vertical mixing: A review and a model with a nonlocal boundary layer parameterization. Rev. Geophys. 32: 363-403. https://doi.org/10.1029/94RG01872

Madec, G., R. Bourdallé-Badie, J. Chanut, E. Clementi, A. Coward, C. Ethé, et al. 2019. NEMO ocean engine. https://doi.org/10.5281/ZENODO.1464816

Madec, G., R. Bourdallé-Badie, J. Chanut, E. Clementi, A. Coward, C. Ethé, et al. 2022. NEMO ocean engine. https://doi.org/10.5281/zenodo.633465

Marshall, J., and F. Schott. 1999. Open-ocean convection: Observations, theory and models. Rev. Geophys. 37: 1-64. https://doi.org/10.1029/98RG02739

Mathiot, P., A. Jenkins, C. Harris and G. Madec. 2017. Explicit representation and parametrised impacts of under ice shelf seas in the z* coordinate ocean model NEMO3.6. Geosci. Model Dev. 10, 2849–2874. https://doi.org/10.5194/gmd-10-2849-2017

Morales Maqueda, M. A., A. J. Willmott, and N. R. T Biggs. 2004. Polynia dynamics: A review of observations and modeling. Rev. Geophys. 42: RG1004. https://doi.org/10.1029/2002RG000116

Morel, A. 1988. Optical modeling of the upper ocean in relation to its biogenous matter content (case I waters). J. Geophys. Res. Oc. 93, 10749-10768. https://doi.org/10.1029/JC093iC09p10749

Moum, J. N., W. D. Smyth, K. G. Hughes, D. Cherian, S. J. Warner, B. Bourlès, P. Brandt, and M. Dengler. 2023. Wind dependencies of deep cycle turbulence in the equatorial cold tongues. J. Phys. Oceanogr. 53:1979–1995. https://doi.org/10.1175/JPO-D-22-0203.1

Perrot M., and F. Lemarié. 2025. Energetically consistent eddy-diffusivity mass-flux convective schemes: 2. Implementation and evaluations in an Oceanic Context. J. Adv. Model. Earth Sys. 17: e2024MS004616. https://doi.org/10.1029/2024MS004616

Perrot M., F. Lemarié, and T. Dubos. 2024. Energetically consistent eddy-diffusivity mass-flux convective schemes: 1. Theory and models. J. Adv. Model. Earth Sys. 17: e2024MS004273. https://doi.org/10.1029/2024MS004273

Piron, A., V. Thierry, H. Mercier and G. Caniaux. 2017. Gyre-scale deep convection in the subpolar North Atlantic Ocean during winter 2014–2015, Geophys. Res. Lett. 44: 1439–1447. https://doi.org/10.1002/2016GL071895

Ramadan, A., G. L. Wagner, C. Hill, J.-M. Campin, V. Churavy, T. Bresard, et al. 2020. Oceananigans.jl: Fast and friendly geophysical fluid dynamics on GPUs. J. Open Source Softw. 5: 2018. https://doi.org/10.21105/joss.02018

Rio, C., F. Hourdin, F. Couvreux, and A. Jam. 2010. Resolved versus parametrized Boundary-Layer plumes. part II: Continuous formulations of mixing rates for Mass-Flux schemes. Boundary-Layer Meteorol. 135: 469–483. https://doi.org/10.1007/s10546-010-9478-z

Rodgers, K. B., O. Aumont, S. E. Mikaloff Fletcher, Y. Plancherel, L. Bopp, C. de Boyer Montégut, D. Iudicone, R. F Keeling, G. Madec and R. Wanninkhof. 2014. Strong sensitivity of Southern Ocean carbon uptake and nutrient cycling to wind stirring. Biogeosc. 11: 4077-4098. doi:10.5194/bg-11-4077-2014

Sathyendranath, S., R. J. W. Brewin, C. Brockmann, V. Brotas, B. Calton, A. Churpin, P. Cipollini, A. B. Couto, J. Dingle, R. Doerffer, et al. 2019. An Ocean-Colour Time Series for Use in Climate Studies: The Experience of the Ocean-Colour Climate Change Initiative (OC-CCI). Sensors. 19, 4285. https://doi.org/10.3390/s19194285

Schott, F., M. Visbeck, U. Send, J. Fischer, L. Stramma, and Y. Desaubies. Observations of deep convection in the Gulf of Lions, northern Mediterranean, during the winter of 1991/92. J. Phys. Oceanogr. 26:505-524. https://doi.org/10.1175/1520-0485(1996)026<0505:OODCIT>2.0.CO;2

Shay, T. J, and M. C. Gregg. 1986. Convectively driven turbulent mixing in the upper ocean. J. Phys. Oceanogr. 16: 1777-1798. https://doi.org/10.1175/1520-0485(1986)016,1777:CDTMIT.2.0.CO;2.

Siebesma, A. P., C. S. Bretherton, A. Brown, A. Chlond, J. Cuxart, P. G. Duynkerke, et al. 2003. A large eddy simulation intercomparison study of shallow cumulus convection. J. Atm. Sci. 60: 1201–1219. https://doi.org/10.1175/1520-0469(2003)60<1201:ALESIS>2.0.CO;2

Storkey, D., A. T. Blaker, P. Mathiot, A. Megann, Y. Aksenov, E. W. Blockley, D. Calvert, T. Graham, H. T. Hewitt, P. Hyder, T. Kuhlbrodt, J. G. L. Rae, and B. Sinha. 2018. UK Global Ocean GO6 and GO7: a traceable hierarchy of model resolutions. Geosci. Model Dev. 11: 3187-3213. https://doi.org/10.5194/gmd-11-3187-2018

Tomita, H., K. Kutsuwada, M. Kubota, and T. Hihara. 2021. Advances in the estimation of global surface net heat flux based on satellite observation: J-OFURO3 V1.1. Front. Mar. Sci. 8: https://doi.org/10.3389/fmars.2021.612361

Tréguier A.-M., C., de Boyer Montégut, A. Bozec, E. P. Chassignet, B. Fox-Kemper, A. McC. Hogg, D. Iovino, A. E. Kiss, J. Le Sommer, Y. Li, P. Lin, C. Lique, H. Liu, G. Serazin, D. Sidorenko, Q. Wang, X. Xiu, and S. Yearger. 2023. The mixed-layer depth in the Ocean Model Intercomparison Project (OMIP): impact of resolving mesoscale eddies. Geosci. Model Dev. 16: 3849-3872. https://doi.org/10.5194/gmd-16-3849-2023, 2023

Våge, K., R. S. Pickart, V. Thierry, G. Reverdin, C. M. Lee, B. Petrie, T. A. Agnew, A. Wong, and M. H. Ribergaard. 2009. Surprising return of deep convection to the subpolar North Atlantic Ocean in winter 2007-2008. Nat. Geosci. 2: 67-72. https://doi.org/10.1038/ngeo382

Vancoppenolle, M., C. Rousset, E. Blockley, Y. Aksenov, D. Feltham, T. Fichefet, G. Garric, V. Guémas, D. Iovino, S. Keeley, G. Madec, F. Massonnet, J. Ridley, D. Schroeder, and S. Tiesche. 2023. SI3, the NEMO Sea Ice Engine. https://doi.org/10.5281/zenodo.7534900

Vreugdenhil, C. A., and B. Gayen. 2021. Ocean Convection. Fluids. 6: 360. https://doi.org/10.3390/fluids6100360

Woolnough, S. J., F. Vitart, and M. A. Balmaseda. 2007. The role of the ocean in the Madden-Jullian Oscillation: implications for MJO prediction. Quat. J. Roy. Meteor. Soc. 133: 117-128. https://doi.org/10.1002/qj.4

Yashayaev, I., and J. W. Loder .2017. Further intensification of deep convection in the Labrador Sea in 2016. Geophys. Res. Lett. 44: 1429–1438. https://doi.org/10.1002/2016GL071668

Zhang, J., R. W. Schmitt, and R. X. Huang. Sensitivity of the GFDL modular ocean model to parameterization of double-diffusive processes. 1998. J. Phy. Oceanogr. 28 589-605. https://doi.org/10.1175/1520-0485(1998)028<0589:SOTGMO>2.0.CO;2

Zhang, Q, B. Liu, S. Li, and T. Zhou. 2023. Understanding models' global sea surface temperature bias in mean state: From CMIP5 to CMIP6. Geophys. Res. Lett. 50: e2022GL100888. https://doi.org/10.1029/2022GL100888